Master's thesis

NTNU
Norwegian University of Science and Technology
Faculty of Natural Sciences
Department of Physics

Mette Wirak

Spin dynamics in magnetic structures

A numerical study

Master's thesis in Nanotechnology
Supervisor: Arne Brataas, Alireza Qaiumzadeh
June 2019

NTNU
Norwegian University of
Science and Technology

Mette Wirak

Spin dynamics in magnetic structures

A numerical study

Master's thesis in Nanotechnology
Supervisor: Arne Brataas, Alireza Qaiumzadeh
June 2019

Norwegian University of Science and Technology
Faculty of Natural Sciences
Department of Physics

NTNU
Norwegian University of
Science and Technology

Preface

This work follows a specialisation project done in the autumn of 2018. The theoretical section concerning ferromagnets will be based on that work, as well as the general discussion of numerical methods. The simulation results of ferromagnetic domain walls and skyrmions are taken directly from the project thesis, while the discussion has been rewritten and adapted to this thesis. All material concerning antiferromagnets is new and independent work from the spring of 2019.

I'd like to express my graditude towards my supervisors, Arne Brataas and Alireza Qaiumzadeh, for both giving me the opportunity to work in their group and for all the guidance and motivation along the way. I'd also like to thank Xiansi Wang, who's been my go-to guy for all things within numerics and simulations.

Abstract

Spintronics, the fundament of this thesis, proposes a way of doing data storage more efficiently and faster. The field is based on the quantum mechanical property of *spin*, which can be transferred through spin waves without moving the particles themselves. This thesis will consider movement caused by spin waves of stable magnetic structures, specifically domain walls and skyrmions.

The analytical work is based on treating the atomic spins as classical vectors, using descriptions of both classical and quantum mechanical spin interactions. From this, the Landau-Lifshitz-Gilbert equation is derived, decribing the motion of an ordered spin system. This is subsequently combined with thermodynamical concepts, such as to give expressions for the expected antiferromagetic skyrmion velocity in a temperature gradient. Importance is here put on the assumptions made during the derivation, so that the result can be understood and adapted to also consider spin waves generated without the thermal gradient.

Running micromagnetic simulations, antiferromagnetic skyrmion motion is successfully obtained using both a temperature gradient and a localised magnetic field. The former gives skyrmion motion with a high variation, due to random thermal fluctuations, with a mean velcity of 8.9 m/s obtained at the highest. The localised magnetic field gives much higher skyrmion velocities, with the maximum mean velocity observed being 103.2 m/s, and is deterministic. Demonstrating that the localised magnetic field does give significant antiferromagnetic skyrmion motion is one of most important results of the thesis, as references of that being done in numerical simulations previously have not been found.

A further significant result is the lack of movement in the y-direction. Neither method produced any skyrmion motion perpendicular to the spin waves, which is not in accordance with the analytical predictions. The temperature gradient is prediced to give spin waves of random polarisation and thus no net transport of angular momentum, with the skyrmion maintaining a constant position in y. However, the magnetically induced spin waves are predicted to give differing velocities in y, as determined by the polarisation of the magnetic field applied.

Sammendrag

Spintronikk foreslår en alterativ måte å gjøre datalagring på, som vil kunne være både mer effektiv og raskere. Grunnlaget for forskningsfeltet er den kvantemekaniske egenskapen *spinn*, som gjennom spinnbølger kan forflyttes uten at partiklene selv flyttes på. Denne masteroppgaven ser nærmere på bevegelse av magnetiske strukturer - spesifikt domenevegger og skyrmioner - forårsaket av spinnbølger.

Det analytiske arbeidet baseres på å behandle atomisk spinn som en klassisk vektor, hvor vekselvirkningene mellom spinnene inkluderer både klassiske og kvantemekaniske effekter. Ut ifra dette vil Landau-Lifshitz-Gilbert-ligningen bli utledet, som beskriver utviklingen i ordnede spinnsystemer. Denne blir videre kombinert med termodynamikk for å uttrykke den forventede hastigheten til antiferromagnetiske skyrmioner plassert i en temperaturgradient. I utledningen blir det lagt vekt på antagelser som gjøres, slik at uttrykket for hastighet forstås og kan adapteres til spinnbølger generert ved hjelp av andre krefter enn temperaturgradienter.

I mikromagnetiske simuleringer oppnås bevegelse av antiferromagnetiske skyrmioner, både ved en temperaturegradient og ved et lokalisert magnetisk felt. Førstnevnte gir bevegelse med høy variasjon, grunnet tilfelding termiske fluktuasjoner, og høyeste observerte gjennomsnittshastighet er på 8.9 m/s. Det lokale magnetfeltet er deterministisk og gir høyere hastighet, med høyeste gjennomsnittshastiget observert på 103.2 m/s. Ingen av metodene viste noen bevegelse av skyrmionene i y-retning.

Blant resultatene kan to trekkes frem som særlig viktige. Demonstrasjonen av bevegelse i antiferromagnetiske skyrmioner gjennom spinnbølger generert av lokaliserte magnetfelt sees, og er ikke vist numerisk tidligere, ifølge det forfatteren har funnet. Videre er mangelen av bevegelse i y-retning et viktig punkt, da dette avviker fra de analytiske beregninene. En temperaturgradient genererer spinnbølger med tilfeldig polarisering, hvilket i gjennomsnitt fører til null overført vinkelmoment og at skyrmionet forblir på samme sted i y. De magnetisk genererte spinnbølgene burde imidlertid gi forskjellige hastigheter i y, bestemt av polariseringen til det påsatte magnetiske feltet.

Abbreviations

AFM Antiferromagnetic

DMI Dzyaloshinskii-Moriya Interaction

DW Domain Wall

FM Ferromagnetic

LLG Landau-Lifshitz-Gilbert

Contents

Chapter 1

Introduction

Information has been transferred between people throughout the ages, but the methods for doing so has been a continuous work in progress. First came spoken communication, with the cumulative knowledge of mankind being dependent on individuals' cognitive abilities. Next came various forms of written information, in which the restriction became to the physical location of the information. We are now in the age of digital information.

The transfer of information is currently restricted primarily through the velocity at which digital data can move. In some applications, such as large simulations or calculations done for research purposes, it can also be restricted in the amount of data one is physically able to store.

A motivation for further improving the technology of data storage can be found in considering how information storage is used, including both personal, academic and professional parts of life. Any calculation, any email sent, any simulation, any streaming of a film requires information to be stored and read. Improving how one deals with digital information can thus not only speed up the daily encounters people might have with their cell phones, but can also enable research hitherto hindered by both the speed and the volume of information to be processed. Furthermore, all digital storage requires energy, with 2.5×10^{18} new bytes of data created every day per May 2018 [1], and the promise of Internet of Things to wastly increase upon that number. A more efficient data storage technology would save a significant amount of electrical power, with Forbes Magazine estimating that 3% of the total energy consumption worldwide is used by data centres per December 2017 [2]. Spintronics could be a necessary part of a more environmental-friendly future [3].

A different motivation can be found along the lines of fundamental research. The existence of skyrmions was first predicted theoretically by Thomas Skyrme in the late 1950s [4]. The prediction was made as a mathematical way of explaining the existence of subatomic particles such as neutrons and protons, and was thus discussed along concepts such as quarks and string theory. The structures were first observed through experiments in 2010,

using Lorentz TEM [5]. And antiferromagnetic structures, which will be the main focus of this thesis, has still not been experimentally observed, as antiferromagnetic material are in general more difficult to measure due to their insensitivity to magnetic fields. The motion of magnetic structures is thus a topic which can be contributed to.

1.1 Outline

Devices which store and process information generally do so by defining separate regions, where each regions saves one of two possible values, such that the information can be stored using binary code. Each such region is known as a bit of information, and sequences of bits can store numbers, letters, images. However, in order to make any device which can do so, there are three main things one needs to be able to do [6]:

* Read the value of a bit
* Control the value of a bit
* Move the bit

The focus of this master thesis will lie on the final one of these three points, moving the information. As such, the plan for the thesis will be to first get to know the theoretical landscape which we will use to describe the materials. This will be done in Part I. More specific systems including magnetic structures will then be studied, both analytically and numerically. Part II will look at ferromagnetic domain walls and skyrmions exposed to an electrical current, in which interactions between the electrons in the current and the electrons in the sample material are expected to cause movement of the magnetic structures. The material considered in Part II will consequently be conducting, while part III moves on to insulating antiferromagnetic materials. Skyrmions will here be attempted moved with both a temperature gradient and a magnetic field. Most of the mentioned situations have been looked at before, but no litterature has been found on the latter one mentioned. The motion of antiferromagnetic skyrmions caused by a localised magnetic field as illustrated in figure 1.1, will as such be the results with most importance.

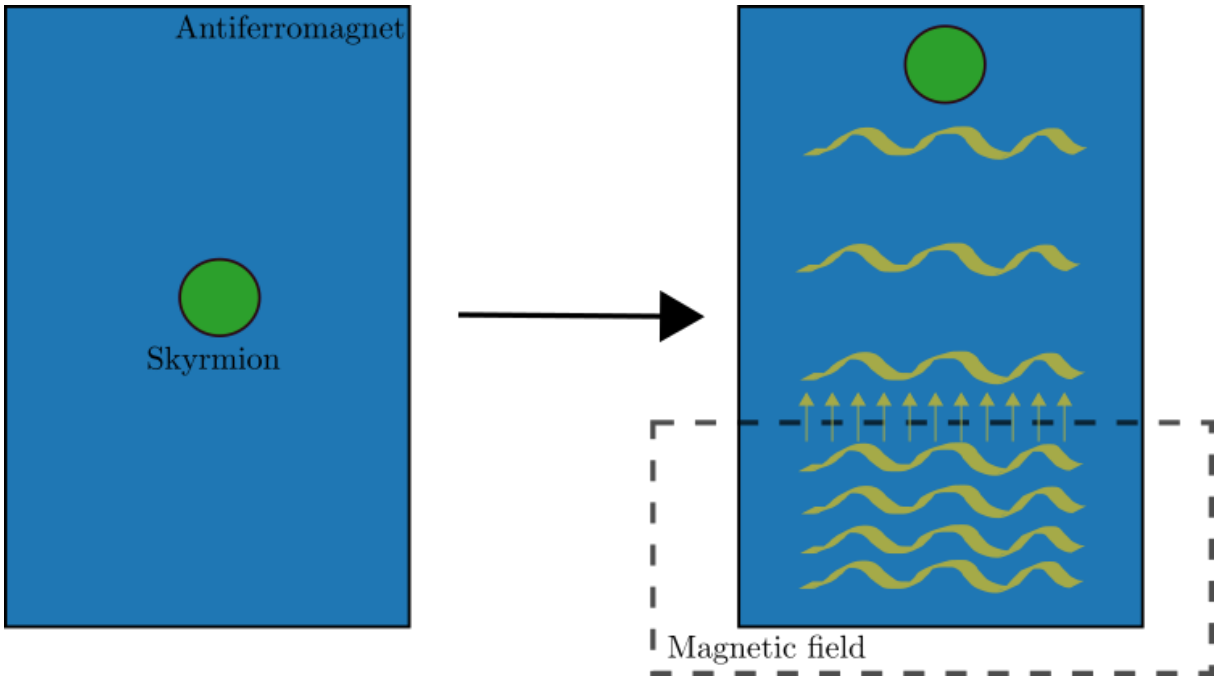

Figure 1.1: Applying a magnetic field to a region of antiferromagnetic material is predicted to induce travelling coherent spin waves, which will cause a skyrmion located elsewhere in the sample to move.

Part I

Theoretical work

Chapter 2

Theory of magnetic materials

From everyday life, the fact that materials have differing magnetic properties is known to most. Some materials stick to the refridgerator door, others do not. Some pans work on an induction stove, others do not.

The magnetic properties of materials relate directly to the spin properties of the atoms making up the material. These spin properties include whether the atoms have a net amount of spin, and how the spins behave in relation to each other as well as in relation to applied forces. This chapter will introduce the terminology and theory with which magnetisation will later be discussed, and mathematical equations which will prove useful.

2.1 The electron spin

The storage of information in electronic devices has traditionally been based on moving electric charges, in the form of delocalised electrons. The presence of an electron current signifies one state, the absence another. The drawback of this is that moving particles generate heat through *Joule heating*. The generated heat must be dissipated in the device to keep the operating temperature sufficiently low - a problem which is often mitigated with the use of heat sinks. The required area of heat sinks coupled with a higher sensitivity to heat in the nano-scaled regime demands new methods of engineering.

Spintronics - spin electronics - instead relies on the quantum mechanical property of electrons known as spin. It was first derived in the 1920's , in the interface between quantum mechanics and special relativity [7, 8]. The name was given on the basis that its behaviour could be explained by a charge spinning about its own axis. Assuming the negative charge to be evenly distributed over the volume of the electron, electromagnetics gives that a magnetic field would be created. This field could take one of two direction - as the electron could be spinning either clockwise or counter-clockwise. Although that physical description has been proven false, it provides a simple intuitive understanding,

and the name has stuck [9]. The property is nontheless closely related to magnetism through the *intrinsic angular magnetic moment* ($\mathbf{m}_s$) of electrons, as given in equation 2.1, where γ is the gyromagnetic ratio and $\mathbf{S}$ is the spin [10].

$$\mathbf{m}_s = \gamma \mathbf{S} \tag{2.1}$$

Spintronics avoids generating heat by differentiating between charge currents and spin currents. The former is the transport of a net amount of electric charge from one place to another. The most common example of this is electrons moving through a wire, bringing their negative electrical charge with them. The other type of current is one which transports a net amount of spin, not charge. This can be done by transferring angular momentum between atoms.

2.2 Magnetic materials

In choosing materials for a spintronics device, the first requirement is that the spins already exist in some order. This allows the magnetisation of the material to be easily controllable. The two types of magnetic materials used are therefore ferromagnetic and antiferromagnetic materials, as illustrated in figure 2.1.

Ferromagnets display a large net magnetisation in their ground state, caused by the sum of the individual magnetic moments of the atoms. A magnetic field is thus present around the material. In states of higher energy, the spins will fluctuate gradually more around their relaxed positions. At the Curie temperature, the kinetic energy to overrule the potential energy and the material behaves as a paramagnet with randomised spin orientations. The value of the Curie temperature is material dependent.

Antiferromagnets have staggered magnetisation, with neighbouring spins being oppositely aligned. A bulk of an antiferromagnetic (AFM) material in its ground state will thus not have a net magnetisation, as the individual magnetic moments from neighbouring atoms cancel each other out. A common description of an AFM system is having two interpenetrating ferromagnetic sublattices, A and B. Spins in sublattice A are of the same strength, but opposite direction, to spins in sublattice B. Equivalently to ferromagnets, a critical temperature exists above which the AFM material behaves as a paramagnet, here called the Néel temperature.

The transition from disordered to ferro-/antiferromagnetic is a second order phase transition [11], and can be observed through an *order parameter*. An order parameter can be any measurable property, with the value of which one can determine the phase a material is currently in. With $\mathbf{m}_1$ and $\mathbf{m}_2$ as two neighbouring spins, a magnetisation and a staggered magnetisation order parameter can be defined as

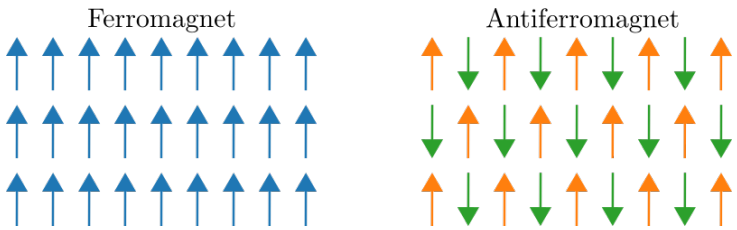

Figure 2.1: Spin configuration in uniform ferromagnetic and antiferromagnetic materials.

$$\mathbf{m} = \frac{\mathbf{m}_2 + \mathbf{m}_1}{|\mathbf{m}_2 + \mathbf{m}_1|} \quad \text{and} \quad \mathbf{n} = \frac{\mathbf{m}_2 - \mathbf{m}_1}{|\mathbf{m}_2 - \mathbf{m}_1|} \tag{2.2}$$

respectively. It can be seen that, in their relaxed states, a ferromagnet will have $|\mathbf{m}| = 1$ and $|\mathbf{n}| = 0$, while an antiferromagnet will give the opposite. Above the critical temperatures, both order parameters will be 0 when averaged over a sufficiently large area.

Both ferro- and antiferromagnets are used in spintronic devices. Ferromagnets have traditionally been more easily controlled, as their magnetic moment is easy to measure, and the spins are sensitive to external magnetic fields. Antiferromagnets do not propagate an external magnetic field to the surroundings, allowing for more compactly packed components. However, as such they are also harder to affect with external magnetic fields, and alternative methods for controlling the spin value are needed. An advantage of antiferromagnets is that the switching between spin states is observed to be much faster, with THz values compared to GHz swithing frequencies in ferromagnets [12, 13].

2.3 A mathematical description of spin interactions

Any physical system will optimally be in its state of minimum free energy. The free energy of the spins of atoms can be described through the systems Hamiltonian, looking at the sum of the interactions the spins will take part in. This can be done either through individual spins (atomistically), or by describing the fields generated by different types of forces (micromagnetically). As the models both have their advantages in certain situations, equations describing both will be given [14].

The most dominant interactions present in a general spin system are listed in equation 2.3, and will in the following sections be discussed individually.

$$\mathcal{H} = \mathcal{H}_{ex} + \mathcal{H}_{DM} + \mathcal{H}_{ani} + \mathcal{H}_{dd} + \mathcal{H}_{ext} \tag{2.3}$$

2.3.1 Heisenberg exchange interaction

The Heisenberg exchange interaction - first desribed by Heisenberg i 1924 - is a quantum mechanical effect which determines the ordering in ferro- and antiferromagnets. Its origin

lies in the interaction between electrons in neighbouring atoms, and in the Pauli exclusion principle [15]. The result of the interaction is that, for some materials, the energy is lower when the spins are aligned in a parallel/antiparallel manner. This is expressed in equation 2.4 through the dimensionless unit vectors $\mathbf{S}_i$ and the material dependent exchange parameter J_{ij}. As shown through the indices, J can take different values depending on the specific interaction looked at, but for this thesis the interaction will be assumed isotropic. In simulations it will also be restricted to only include nearest neighbour-interactions. The stiffness parameter A is the micromagnetic equivalent to J_{ij}, expressed in equation 2.5. It is be proportional to the exchange parameter as well as the atomic spacing.

The Heisenberg exchange interaction is the most dominant of the spin energy interactions. It determines whether neighbouring spins align parallel or antiparrallel manner through the sign of the exchange constant. $J_{ij} < 0$ makes an antiferromagnet, while $J_{ij} > 0$ makes a ferromagnet [14].

$$\mathcal{H}_{ex} = -\frac{1}{2}\sum_{i,j} J_{ij}\mathbf{S}_i \cdot \mathbf{S}_j \tag{2.4}$$

$$\mathcal{H}_{ex} = \int A(\nabla \mathbf{m})^2 d\mathbf{r} \tag{2.5}$$

2.3.2 Dzyaloshinskii-Moriya interaction

Some materials, though having a negative exchange constant and consequently being antiferromagnets, exhibit a weak ferromagnetic behaviour in their ground state. This was described phenomologically by Dzyaloshinskii, and explained by Moriya as being an effect of the quantum mechanical spin orbit interaction [16]. The magnetic moment of an atom consists of both the intristic magnetic moment of the elemental particles, and the magnetic moment created by the electron orbits in space. Dzyaloshinskii-Moriya interaction (DMI) is related to the interplay between these two. The antiferromagnetic materials which exhibit this slight ferromagnetic behaviour are described as canted antiferromagnets, as their spins will all be slightly tilted.

DMI can in equations 2.6 and 2.7 be seen to have a different preferred orientation between neighbouring moments than the Heisenberg exchange interaction, as the lowest energy is here obtained with perpendicularly aligned spins. However, DMI only takes effect in systems with reduced symmetry. Reduced symmetry refers to whenever there is an non-uniformity in the system, such as imperfections in the crystal, or magnetic structures such as domain walls or skyrmions[10]. A common occurrence of strong DMI is also at the interface between different materials, such as a magnetic thin film being formed next to heavy elements.

$$\mathcal{H}_{DMI} = -\mathbf{D}_{12} \cdot (\mathbf{S}_1 \times \mathbf{S}_2) \tag{2.6}$$

The orientation of $\mathbf{D}_{ij}$ will depend on the considered system. Bulk DMI is parallel to the vector separating two spins, and exists in some magnetic materials which have lacking bulk inversion symmetry. A different DMI is the interfacial one, occuring in thin layers of magnetic materials which lack structural inversion symmetry. This will often take place with spins located close to a material with high spin-orbit coupling. $\mathbf{D}$ will then be perpendicular to both the vector between the interacting spin and to the plane of the interface. Considering a ferromagnet with bulk DMI and interfacial DMI in the continuum limit, equation 2.6 can be rewritten to

$$\mathcal{H}_{DMI}^{bulk} = \int D\mathbf{m} \cdot (\nabla \times \mathbf{m}) d\mathbf{r}, \tag{2.7}$$

$$\mathcal{H}_{DMI}^{int} = \int D\mathbf{m} \cdot (\hat{\mathbf{z}} \times \mathbf{m}) d\mathbf{r}, \tag{2.8}$$

respectively [10]. The latter equation is written for a material interface in the xy-plane.

2.3.3 Anisotropy interaction

Atomic spins are located in a crystallographic lattice, and very often the lattice will have orientations of the magnetic moments which are energetically favourable [17]. The interplay between crystallography and magnetic moments is referred to as the *magnetic anisotropy interaction*, and takes different forms for the different crystal structures. The simplest form is that given in equations 2.9 and 2.10, which describe a system with uniaxial anisotropy.

$$\mathcal{H}_{ani} = -K \sum_i (\mathbf{S}_i \cdot \mathbf{e})^2 \tag{2.9}$$

$$\mathcal{H}_{ani} = -\int K(\mathbf{m} \cdot \mathbf{e})^2 \tag{2.10}$$

K is here a material dependent anisotropy constant, while $\mathbf{e}$ is an axis referring to the direction of the anisotropy.

Uniaxial anisotropy occurs for hexagonal and tetragonal crystals, and is defined by having one preferred direction of the magnetisation, known as the easy axis $\mathbf{e}$. The state of lowest energy will have all spins aligned in the direction of the easy axis. It is also possible for

a material to have one direction which is least energetically favourable, known as a hard axis. The difference between the two uniaxial anisotropies can be seen in the sign of K, where a positive value gives an easy axis and a negative value gives a hard axis. It is also possible for materials to have a combination of different anisotropies.

2.3.4 Dipole interaction

The classical dipole interaction is also present in spin systems, abbreviated as $\mathcal{H}_{dd}$ in the equation for the total Hamiltonian. In general, dipoles attempt to align themselves in an antiparallel manner, as to minimise the magnetic field surrounding them. This will also occur with spins. However, the strength of the dipole interaction has been measured to be on the order of 6.25×10^{-2} meV between atomic dipoles kept at a 1 angstom distance from each other. The Heisenberg exchange interaction in the same situation is on the order of 6.25 meV [15]. In short ranges, the dipole interaction can thus be considered negligible.

Considering a longer range, the relation between these strengths changes. While only including the nearest neighbour interaction will often be sufficient for the Heisenberg exchange interaction, the strength of the dipole interaction decreases exponentially with distance from the dipoles. The dipole interaction will thus become increasingly important in large samples, and is an important driving force in magnetic domain formation [14].

2.3.5 Zeeman interaction

The last mentioned interaction, $\mathcal{H}_{ext}$, is the effect on the quantum mechanical energy levels due to an external magnetic field $\mathbf{B}_{ext}$. Eigenstates which are degenerate in their ground state might have different magnetic moments according to their spins, and the external magnetic field will cause a hyperfine splitting of the states. This effect is known as the Zeeman interaction [14].

2.4 Deriving the FM equation of motion

Central in the work for this thesis is the ability to describe a dynamic spin system, not only its ground state. To do so, Lagrangian mechanics will be used with the energy interactions discussed above. Considering a magnetic moment $\mathbf{m}$, the Lagrangian of a general spin system can be written as

$$\mathcal{L}_0 = \int (T - U) d\mathbf{r} = \int L_0 d\mathbf{r}, \tag{2.11}$$

where $T = T(\mathbf{m}, \dot{\mathbf{m}})$ is the kinetic energy of the system, and $U = U(\mathbf{m}, \nabla\mathbf{m})$ is the potential energy of the system. U will thus here relate to the energy interactions discussed in the previous section. L_0 is the Lagrangian expressed as a density function. Wanting to find the stable state of the system with regard to the order parameter, the Euler Lagrange equations can be utilised. These give the functional derivative of $\mathcal{L}$, written as

$$\frac{\partial}{\partial x_i}\frac{\partial \mathcal{L}}{\partial(\partial q/\partial x_i)} = \frac{\partial \mathcal{L}}{\partial q}. \tag{2.12}$$

Here $q = \mathbf{m}$, $i \in 0, 1$ and $x_{0,1} = t, \mathbf{r}$. Furthermore, the order parameter is defined to have a constant length of 1. Including this as a constraint in equation 2.11 gives

$$\mathcal{L} = \mathcal{L}_0 + \lambda(\mathbf{m}^2 - 1), \tag{2.13}$$

where λ is a Lagrange multiplier.

Some dissipation will occur in the system, in the form of lattice vibrations, spin waves and electron excitation. Instead of describing each of these in an exact manner, a phenomological energy dissipation term can be added to 2.12. In this way, although the underlying mechanisms are not specifically accounted for, the resulting damping of the spins is included [10]. The most common such function to use is the Rayleigh dissipation function, which can here be written as

$$\mathcal{R} = \frac{\alpha}{2}\int \dot{\mathbf{m}}^2 d\mathbf{r}. \tag{2.14}$$

The phenomological Gilbert damping constant α is the degree of damping in the system, with values ranging from 0 to 1. The Euler-Lagrange equation, including the dissipation and being expressed in densities, is

$$\frac{\partial L}{\partial q} - \frac{\partial}{\partial x_i}\frac{\partial L}{\partial(\partial q/\partial x_i)} + \lambda\frac{\partial(q^2-1)}{\partial q} = \frac{\partial R}{\partial(\partial q/\partial x_0)}. \tag{2.15}$$

By definition it is known that the kinetic energy is independent of $\nabla\mathbf{m}$, while the potential energy is independent of $\partial_t\mathbf{m}$. This simplifies the equation to

$$\left(\frac{\partial T}{\partial \mathbf{m}} - \partial_t\frac{\partial T}{\partial \dot{\mathbf{m}}}\right) - \left(\frac{\partial U}{\partial \mathbf{m}} - \nabla\frac{\partial U}{\partial \nabla\mathbf{m}}\right) + 2\lambda\mathbf{m} = \alpha\dot{\mathbf{m}}. \tag{2.16}$$

With the aim of further simplifying the equation, it can be multiplied with $(\mathbf{m}\times)$. As the cross product of any vector with itself is zero, the equation then becomes

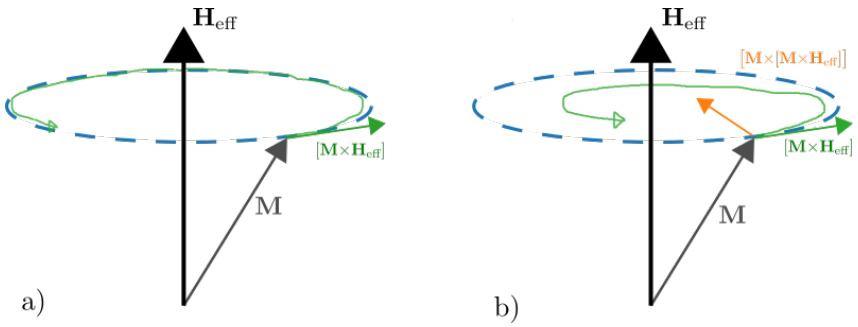

Figure 2.2: The motion of a magnetic moment ($\mathbf{M}$) in an effective magnetic field density ($\mathbf{H}_{eff}$), according to the Landau-Liftshitz-Gilbert equation. a) shows the motion caused by only the processional term, while b) also includes the damping term [18].

$$\begin{aligned} \mathbf{m} \times \left(\frac{\partial T}{\partial \mathbf{m}} - \partial_t \frac{\partial T}{\partial \dot{\mathbf{m}}}\right) - \mathbf{m} \times \left(\frac{\partial U}{\partial \mathbf{m}} - \nabla \frac{\partial U}{\partial \nabla \mathbf{m}}\right) + 2\lambda \mathbf{m} \times \mathbf{m} &= \alpha \mathbf{m} \times \dot{\mathbf{m}}, \\ \mathbf{m} \times \left(\frac{\partial T}{\partial \mathbf{m}} - \partial_t \frac{\partial T}{\partial \dot{\mathbf{m}}}\right) - \mathbf{m} \times \left(\frac{\partial U}{\partial \mathbf{m}} - \nabla \frac{\partial U}{\partial \nabla \mathbf{m}}\right) + 0 &= \alpha \mathbf{m} \times \dot{\mathbf{m}}. \end{aligned} \tag{2.17}$$

It can be shown that the first term, involving the kinetic energy, can be rewritten to simply $\dot{\mathbf{m}}$ [14]. Furthermore, the effective field experienced by the magnetic moment $\mathbf{m}$ can be defined as

$$\mathbf{H}_{eff} \equiv -\frac{1}{\gamma} \frac{\delta U}{\delta \mathbf{m}}, \tag{2.18}$$

where γ again is the gyromagnetic ratio. The equation of motion then simplifies to

$$\dot{\mathbf{m}} = -\gamma \mathbf{m} \times \mathbf{H}_{eff} + \alpha \mathbf{m} \times \dot{\mathbf{m}}. \tag{2.19}$$

Using vector identities, an equivalent formulation can be given as

$$\dot{\mathbf{m}} = -\frac{\gamma}{1+\alpha^2} \mathbf{m} \times \mathbf{H}_{eff} - \frac{\gamma \alpha}{1+\alpha^2} \mathbf{m} \times (\mathbf{m} \times \mathbf{H}_{eff}). \tag{2.20}$$

Equations 2.19 and 2.20 are both formulations of the ferromagnetic Landau-Liftshitz-Gilbert (LLG) equation, describing the motion of a magnetic moment in a ferromagnet.

The first term in the LLG equation is referred to as the processional term. When considering only this term, the motion of the order parameter would be an everlasting revolution around the effective magnetic field. The second term, known as the damping term, includes the fact that an undisturbed system will tend gradually towards having the order parameter aligned with the effective magnetic field. An illustration of this concept is given in figure 2.2.

Until now, the discussion has only considered an isolated system. In a more general form, the LLG equation is often written as

$$\dot{\mathbf{m}} = -\frac{\gamma}{1+\alpha^2}\mathbf{m} \times \mathbf{H}_{eff} - \frac{\gamma\alpha}{1+\alpha^2}\mathbf{m} \times (\mathbf{m} \times \mathbf{H}_{eff}) + \boldsymbol{\tau}, \tag{2.21}$$

where $\boldsymbol{\tau}$ represent the effect of any forces applied to the system.

2.5 Deriving the AFM equation of motion

Looking at an antiferromagnet, a slightly different approach to finding an equation of motion is used, in which both the magnetisation order parameter and the staggered order parameter are utilised [10]. Starting from the free energy of a one dimensional chain of atoms, one can write

$$U = -J \sum_{i=1}^{2N-1} \mathbf{S}_i \cdot \mathbf{S}_{i+1} - \sum_{i=1}^{2N} (-1)^i \mathbf{D} \cdot (\mathbf{S}_i \times \mathbf{S}_{i+1}) - K_0 \sum_{i=1}^{2N} S_{i,z}^2, \tag{2.22}$$

with $J < 0$. S_i here represents a spin by a classical vector, as much of the treatment has done before as well. Wanting to express this instead through the order parameters, we define

$$\mathbf{m}_i = (\mathbf{S}_{2i-1} + \mathbf{S}_{2i})/2S, \tag{2.23}$$

$$\mathbf{l}_i = (\mathbf{S}_{2i-1} + \mathbf{S}_{2i})/2S. \tag{2.24}$$

The spins have thus been paired up into antiferromagnetic unit cells. The spin $\mathbf{S}$ should always have a constant magnitude, giving the consequent relations $\mathbf{m}^2 + \mathbf{l}^2 = 1$ and $\mathbf{m}_i \cdot \mathbf{l}_i = 0$. Rewriting the equation above, one can express the spin values as

$$\mathbf{S}_{2i-1} = S(\mathbf{m}_i + \mathbf{l}_i), \tag{2.25}$$

$$\mathbf{S}_{2i} = S(\mathbf{m}_i - \mathbf{l}_i). \tag{2.26}$$

Applying these expressions into equation 2.22 and simplifying the result using vector identities, one is left with

$$
\begin{aligned}
U = &- JS^2 \sum_{i=1}^{N-1} (3\mathbf{m}_i^2 + \mathbf{m}_{i+1}^2 - 2) - \frac{JS}{2} \sum_{i=1}^{N-1} \left((\mathbf{l}_{i+1} - \mathbf{l}_i)^2 - (\mathbf{m}_{i+1} - \mathbf{m}_i)^2 \right) \\
&- JS^2 \sum_{i=1}^{N-1} \left(\mathbf{m}_i \cdot (\mathbf{l}_{i+1} - \mathbf{l}_i) - \mathbf{l}_i \cdot (\mathbf{m}_{i+1} - \mathbf{m}_i) \right) - JS^2 \left(\mathbf{m}_N^2 - \mathbf{l}_N^2 \right) \\
&+ S^2 \sum_{i=1}^{N-1} \mathbf{D} \cdot [\mathbf{m}_i \times (\mathbf{l}_i + \mathbf{l}_{i+1}) - \mathbf{l}_i \times (\mathbf{m}_i + \mathbf{m}_{i+1})] \\
&+ S^2 \sum_{i=1}^{N-1} \mathbf{D} \cdot [\mathbf{m}_i \times (\mathbf{m}_{i+1} - \mathbf{m}_i) - \mathbf{l}_i \times (\mathbf{l}_{i+1} - \mathbf{l}_i)] - 2K_0 S^2 \sum_{i=1}^{N} \left(m_{i,z}^2 + li + 1, z^2 \right)
\end{aligned}
\tag{2.27}
$$

Looking at a large number of spins N and a small unit cell length $2a$, the limit can be taken in which the sums can be replaced by integrals, and the individual $\mathbf{m}_i$ by a vector field $\mathbf{m}(x)$, done through

$$
\sum_{i=1}^{N-1} \longrightarrow \frac{1}{2a} \int dx \quad \text{and} \quad \mathbf{m}_{i+1} - \mathbf{m}_i \longrightarrow 2a \partial_x \mathbf{m}. \tag{2.28}
$$

Using this, and equivalently for $\mathbf{l}(x)$, in the expression for free energy, one obtains

$$
\begin{aligned}
U[\mathbf{m}, \mathbf{l}] = &- \frac{JS^2}{2a} \int [4\mathbf{m}^2 + 2a^2 (\partial_x \mathbf{l})^2 - 2a^2 (\partial_x \mathbf{m})^2 + 2a(\mathbf{m} \cdot \partial_x \mathbf{l} - \mathbf{l} \cdot \partial_x \mathbf{m})] dx \\
&+ S^2 \int [\frac{2}{a} \mathbf{D} \cdot (\mathbf{m} \times \mathbf{l}) + \mathbf{D} \cdot (\mathbf{m} \times \partial_x \mathbf{m}) - \mathbf{D} \cdot (\mathbf{l} \times \partial_x \mathbf{l})] dx \\
&- \frac{K_0 S^2}{a} \int [(\mathbf{m} \cdot \hat{\mathbf{z}})^2 + (\mathbf{l} \cdot \hat{\mathbf{z}})^2] dx.
\end{aligned}
\tag{2.29}
$$

Consequences from the continuum model used here are also that the boundary term in equation 2.27 becomes negligible, and that $\mathbf{m}(x)^2$ varies slowly in space. A further model, the exchange approximation, will also be used. The model states that $|J| >> |K|$, with the consequence that the spins will be deviating only slightly from an antiparallel configuration. In magnetic structures, the domain walls will be wide. In an antiferromagnet, this also inferres that $\mathbf{m}^2$ will be much smaller than $\mathbf{l}^2$. Using this we introduce the staggered unit vector $\mathbf{n} = \mathbf{l}/|\mathbf{l}|$. For small deviations from $|\mathbf{m}| = 0$ and $|\mathbf{n}| = 1$, we still have $\mathbf{m}^2 + \mathbf{n}^2 = 1$ and $\mathbf{m} \cdot \mathbf{n} = 0$. Considering second order terms of the magnetisation as negligible when in the same term as a staggered order parameter, the free energy can be written as

$$
U[\mathbf{m}, \mathbf{n}] = \int \Big[\frac{1}{2\chi} \mathbf{m}^2 + \frac{A}{2} (\partial_x \mathbf{n})^2 + L\mathbf{m} \cdot \partial_x \mathbf{n} - \frac{K}{2} (\mathbf{n} \cdot \hat{\mathbf{z}})^2 \Big] dx + U_{\text{DMI}}, \tag{2.30}
$$

where the parameters introduced are defined as

$$\chi = \frac{a}{4|J|S^2}, \quad A = 2a|J|S^2, \quad L = 2|J|S^2, \quad K = \frac{2K_0S^2}{a}. \tag{2.31}$$

Considering an atom with one unpaired electron, which is known to have $S = \pm\frac{1}{2}$, this can be simplified into

$$\chi = \frac{a}{|J|}, \quad A = \frac{a|J|}{2}, \quad L = \frac{|J|}{2}, \quad K = \frac{K_0}{2a}. \tag{2.32}$$

The free energy of the DMI has been separated out in equation 2.30, as the formulation used depends on the system one is to consider. The first DM term in equation 2.29 is called the homogeneous Dzyaloshinskii-Moriya interaction, and becomes significant when $\mathbf{D}$ has a component which is parallel to the chain of spins and which is alternating in sign. Its free energy is given by

$$U^h_{\text{DMI}}[\mathbf{m}, \mathbf{n}] = \int \mathbf{d} \cdot (\mathbf{m} \times \mathbf{n}) dx, \tag{2.33}$$

where $\mathbf{d} = (2D_aS^2/a)\hat{\mathbf{x}}$ and D_a is the magnitude of the alternating component. The second DMI term in equation 2.29 is negligible in the continuum limit, and the last term can be either $U^{\text{bulk}}_{\text{DMI}}$ or $U^{\text{int}}_{\text{DMI}}$. The former occurs when $\mathbf{D}||\hat{\mathbf{x}}$. The second takes place when close to an interface between the antiferromagnetic material and a material with a strong spin-orbit coupling, and has $\mathbf{D}||\hat{\mathbf{y}}$. Using $D = |\mathbf{D}|S^2$, the two interactions are given by

$$U^{\text{bulk}}_{\text{DMI}}[\mathbf{m}, \mathbf{n}] = \int D\mathbf{n} \cdot (\hat{\mathbf{x}} \cdot \partial_x \mathbf{n}) dx, \tag{2.34}$$

$$U^{\text{int}}_{\text{DMI}}[\mathbf{m}, \mathbf{n}] = \int D\mathbf{n} \cdot (\hat{\mathbf{y}} \cdot \partial_x \mathbf{n}) dx. \tag{2.35}$$

Now having an expression for the free energy of the system, the Lagrangian of the system can be written as

$$L[\mathbf{m}, \mathbf{n}] = \mathcal{J} \int \partial_t \mathbf{n} \cdot (\mathbf{n} \times \mathbf{m}) dx - U[\mathbf{m}, \mathbf{n}]. \tag{2.36}$$

The first term is here an expression of the kinetic energy in the system, derived Bby Kristiansen [10], while $\mathcal{J} = S/(2a)$ is the one-dimensional density of spin angular momentum. Following the method used in the previous section, with the constraints that $|\mathbf{n}|^2 = 1$ and $\mathbf{m} \cdot \mathbf{n} = 0$, we look at the variation of

$$L[\mathbf{m}, \mathbf{n}] + \int d\mathbf{r} \Big[\lambda_1(|\mathbf{n}|^2 - 1) + \lambda_2 \mathbf{m} \cdot \mathbf{n}\Big], \tag{2.37}$$

with respect to the order parameters. This gives

$$\mathcal{J}(\partial_t \mathbf{n} \times \mathbf{n}) = \frac{\delta U}{\delta \mathbf{m}} - \lambda_2 \mathbf{n}, \tag{2.38}$$

$$\mathcal{J}[2(\mathbf{m} \times \partial_t \mathbf{n}) + (\partial_t \mathbf{m} \times \mathbf{n})] = \frac{\delta U}{\delta \mathbf{n}} - 2\lambda_1 \mathbf{n} - \lambda_2 \mathbf{m}. \tag{2.39}$$

The variation with respect to the Lagrange multipliers should also be included, but this only returns the constraints on $\mathbf{n}$ and $\mathbf{m}$ as are already given. However, it will be useful to look at the partial differentiation with respect to time of the constraints, which gives

$$\partial_t \mathbf{n} \cdot \mathbf{n} = 0, \tag{2.40}$$

$$\partial_t \mathbf{m} \cdot \mathbf{n} + \mathbf{m} \cdot \partial_t \mathbf{n} = 0, \tag{2.41}$$

respectively. We can also define the effetive fields

$$\mathbf{f}_\mathbf{m} = -\frac{1}{\mathcal{J}} \frac{\delta U}{\delta \mathbf{m}} \quad \text{and} \quad \mathbf{f}_\mathbf{n} = -\frac{1}{\mathcal{J}} \frac{\delta U}{\delta \mathbf{n}}. \tag{2.42}$$

Taking the cross product of $\mathbf{n}$ and the first of the differential equations gives

$$\partial_t \mathbf{n} = -\, \mathbf{n} \times \mathbf{f}_\mathbf{m}, \tag{2.43}$$

and the dot product of the same two vectors gives

$$\lambda_2 = -\, \mathcal{J} \mathbf{n} \cdot \mathbf{f}_\mathbf{m}, \tag{2.44}$$

Looking at the second differential equation, the equivalent relations give

$$\partial_t \mathbf{m} = -\mathbf{n} \times \mathbf{f}_\mathbf{n} - \mathbf{m} \times \mathbf{f}_\mathbf{m}. \tag{2.45}$$

The effective fields, defined through the potential energy U, can be written out as

$$\mathcal{J} \mathbf{f}_\mathbf{m} = \frac{1}{\chi} \mathbf{m} - L \partial_x \mathbf{n}, \tag{2.46}$$

$$\mathcal{J} \mathbf{f}_\mathbf{n} = A \partial_x^2 \mathbf{n} + L \partial_x \mathbf{m} + K(\mathbf{n} \cdot \hat{\mathbf{z}}) \hat{\mathbf{z}}. \tag{2.47}$$

The DMI has here not been included in the potential energy, due to its form depending on the system. Should it be included for a given situation, the above equations should be recalculated. Inserting the expression of $\mathbf{f}_\mathbf{m}$ into equation 2.38, it can be seen that $\mathbf{m}$

is only a ghost variable of $\mathbf{n}$. Using this, the Lagrangian density of the system can be written

$$\mathcal{L} = \mathcal{J}^2\chi(\partial_t\mathbf{n})^2 + L\mathcal{J}\chi\mathbf{n}\cdot(\partial_t\mathbf{n}\times\partial_x\mathbf{n}) - \frac{A-2L^2\chi}{2}(\partial_x\mathbf{n})^2 + \frac{K}{2}(\mathbf{n}\cdot\hat{\mathbf{z}})^2. \tag{2.48}$$

This can be rewritten in a simpler manner by defining $\rho = 2\mathcal{J}\chi$ and $A' = A - L^2\chi$. Furthermore, the term $\mathbf{n}\cdot(\partial_t\mathbf{n}\times\partial_x\mathbf{n})$ can be shown to be zero [10]. The resulting Lagrangian becomes

$$\mathcal{L} = \frac{\rho}{2}(\partial_t\mathbf{n})^2 - \frac{A'}{2}(\partial_x\mathbf{n})^2 + \frac{K}{2}(\mathbf{n}\cdot\hat{\mathbf{z}})^2. \tag{2.49}$$

The equation of motion for the staggered order parameter then becomes

$$\mathbf{n}\times\big[-\rho\partial_t^2\mathbf{n} + A'\partial_x^2\mathbf{n} + K(\mathbf{n}\cdot\hat{\mathbf{z}})\hat{\mathbf{z}}\big] = 0. \tag{2.50}$$

Chapter 3

Magnetic structures

In their respective ground states, both ferromagnets and antiferromagnets are uniform. This chapter considers situations in which this is not the case, but which are still stable. Doing so will aim at finding suitable magnetic structures for use in data storage technology, where the suitability is determined primarily by how simple it is to control the motion of the structure. The last section will also look at one of the ways in which one can control magnetic structures in insulators, namely spin currents.

3.1 Domain walls

The simplest, and most common, non-uniformity which may occur in magnetic crystals is magnetic domain walls. The domains here constitute smaller regions in the material in which the magnetisation is uniform, but with the magnetisation direction differing between the different domains. The formation of such structures occurs to minimise the free energy of the system.

With the aim of getting an intuitive understanding of domain formation, one can consider a ferromagnet. Should the material consist of only a single domain, the sum of the magnetic moments from the atoms is large, and a large magnetic field would be propagating from the sample. Should instead the material divide into several magnetic domains, each with a different direction of their magnetic moments, then the external field from the sample would be much smaller. From the discussion of the different interactions it was also mentioned that the dipole interaction, over long ranges, becomes more prominent than the Heisenberg exchange interaction. This again favours domain formation, when the material in question becomes relatively large.

For antiferromagnets, an intuitive understanding can be obtained by considering a system which is initially in the unordered state, by having a temperature well above the Néel temperature. Gradually lowering the temperature, ordered regions will appear randomly

in several regions throughout the sample. Their orientations will be determined by the anisotropy of the material, which in many materials have more than one direction which will minimise the free energy. As the material becomes gradually more ordered, domain walls will occur between the different regions.

Domain walls are defined as the region of transition between two domains, and magnetic domain walls will hence be a region with gradually changing spin directions. The width depends on the material specific interaction constants, but will in a ferromagnet generally lie between 10 and 100 nm [19]. A high DMI constant will give a broad DW, while both high Heisenberg exchange coefficients and high anisotropy constants will favour a narrow one.

There are two types of domain walls, Bloch and Néel. The difference between the two is in which plane the rotation occurs, it being either parallel (Bloch) or perpendicular (Néel) to the domain wall. The type of domain wall which occurs in a given system will be determined by which has the lowest free energy. Considering only the Heisenberg exchange interaction and DMI, the energies of the two walls would be equivalent. However, system anisotropies will often be important, as well as the dimensions of the material and of the domains. On a general note it has been found that Bloch domain walls occur more often in bulk, while Néel domain walls are more frequent in thin films [20]. A further classification of domain walls is the angle between the spins of the domains the wall is separating, where a 180° domain wall is what will most often be considered.

Looking at magnetic structures for use in information storage, domain walls are ceratin to be a part of the unit of information. Either as the domain wall itself being the bit, or as domains being the bit [21]. Either way, the movement of the bit will be determined by the movement of domain walls.

3.2 Skyrmions

To acchieve maximum efficiency, the size of the magnetic structure which is to represent a bit should be minimised. The structure know as a *skyrmion*, either a ferromagnetic or an antiferromagnetic one, is the minimal size of a 180° magnetic domain one can have. A cross section of skyrmions are given in 3.1, where it can be seen to consist of an inner domain (in the figure only one spin wide), a domain wall and an outer domain.

The size of a skyrmion, both the inner domain and the domain wall, depend sensitively on the relative strengths of the Heisenberg exchange interaction, DMI and the anisotropy interaction. Any applied magnetic fields will also be important, but has not been considered here. As both exchange stiffness, DMI and anisotropy are material properties, the size of skyrmions will be characteristic for different materials. However, on a general note they have sizes between 1 and 100 nm in diameter [22]. General trends also show that

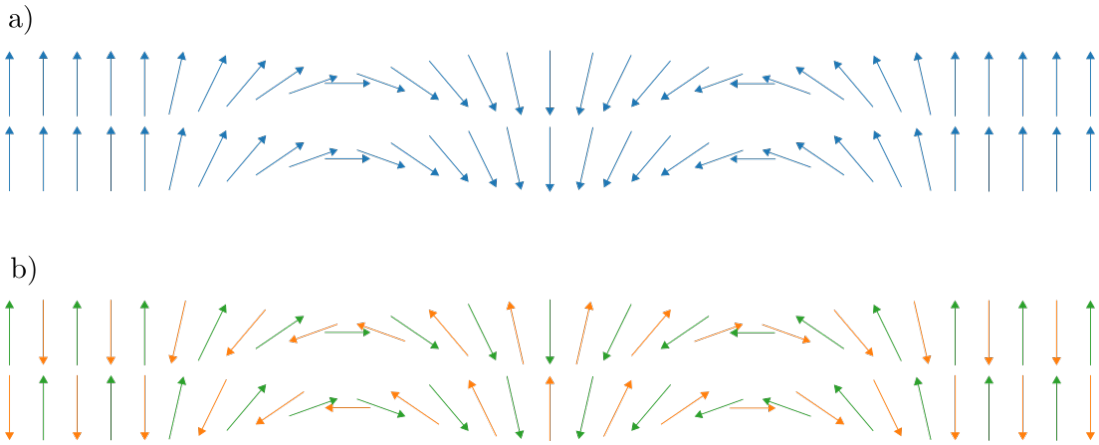

Figure 3.1: Illustration of two skyrmions as seen from the side. a) is ferromagnetic, while b) is antiferromagnetic.

the size of the inner domain decreases with increasing exchange interaction strength, and that both the inner domain size and the domain wall width increase with increasing DMI strength. A derivation of the analytic expression for these sizes based on minimising the free energy of the system as a function of inner domain size (R) and domain wall width (w) of a skyrmion is done by Wang et. al. [22], giving as its result

$$\mathrm{R} = \pi D \sqrt{\frac{A}{16AK^2 - \pi^2 D^2 K}} \tag{3.1}$$

$$\mathrm{w} = \frac{\pi D}{4K} \tag{3.2}$$

Skyrmions are often described as quasi particles, being topologically stable. This originates in their quantised topological number, Q^m, as given in equation 3.3. A situation in which the magnetisation is gradually evened out to give a uniform magnetisation is deemed impossible by the quantisation. Either the skyrmion exists with a topological number of ± 1, or no skyrmion exists [23]. This also holds for an antiferromagnetic skyrmion, though applying equation 3.3 directly would give 0. A more useful expression for antiferromagnets is to consider the topological number in each of the sublattices. This will give $Q^m_A = -Q^m_B = \pm 1$.

$$Q^m = \frac{1}{4\pi} \int d^2\mathbf{r}\mathbf{m} \cdot (\partial_x \mathbf{m} \times \partial_y \mathbf{m}) \tag{3.3}$$

A consequence of the topological number is the topological Hall effect. When exposed to an electric current, the motion of ferromagnetic skyrmions is expected to be along the direction of the current. However, an additional movement in a perpendicular direction has been observed. The direction of the perpendicular motion will be determined by the sign of the topological number, equivalently to the classical Hall effect [23]. It's been found that the angle between the electrical current and the path of the skyrmion can

exceed 30°, and that the velocity of the perpendicular motion depends on the size of the skyrmion, as well as the velocity in the direction of the electrical current.

Skyrmions have been observed in various magnetic thin films, including MnSi, FeGe and $Fe_{1-x}Co_xSi$. It has also been shown experimentally that one can cause them to move by applying electrical currents as low as 10^{-5} A/m^2, much lower than the equivalent value for domain walls, and that one can write and delete skyrmions in a thin film using a scanning tunnelling microscope [24].

Antiferromagnetic skyrmions appear to be highly equivalent to their ferromagnetic counterparts. They are both stable due to their topological isolation. An important difference is that, due to its zero net topological charge, no topological Hall effect will take place. Each of the sublattices will have a net topological charge, but in the material as a whole it is cancelled out. This holds a practical consequence in the use of AFM for information storage purposes, as an AFM skyrmion will travel in a straight line when exerted to an electrical current.

It should be noted that, when considering skyrmions in thin films, they may exist in two forms. A skyrmions lattice can form, in which skyrmions are regularly spaced out all throughout the volume. This only occurs in a narrow part of the phase diagrams of certain materials, and both the external magnetic field and temperature must thus be presicely adapted to acchieve their existence. The other alternative it to have a uniform spin configuration, except for one single isolated skyrmion. The latter is what will be looked at throughout the thesis, both when considering FM and AFM skyrmions.

3.3 Spin waves

Light can be described as travelling electromagnetic waves, sound as travelling waves of air pressure. An equivalence also exists within magnetic energy, known as *spin waves*. In an ordered magnetic material, a spin wave will be observable as a small fluctuation around the ground state. The fluctuations of one spin will influence its neighbours through exchange interaction, and a similar motion will be induced in the neighbour, only slightly delayed. This results in a travelling spin wave. Considering wave-particle duality, the spin wave can also be considered the quasiparticle *magnon* [11].

In figure 3.2 c), the properties of a ferromagnetic spin wave is illustrated. Each spin rotates with the same angular frequency ω, but with a gradually changing phase. It is also seen that a ferromagnetic spin wave will carry a net angular momentum, which is of size $1\hbar$. For an antiferromagnetic lattice, in which both sublattices rotate with the same frequency, a cancellation of the angular momentums of the two sublattices can occurs for linearly polarised spin waves. Circularly polarised spin waves do however carry angular momentum also in antiferromangets [10, 25]. Furthermore, where only right-circulalry

polarised spin waves can exist, both directions are possible for AFM.

The energy needed to excite the ground system can be introduced to the system through temperature, or through both electric and magnetic fields. The method chosen will impact the magnons formed. Temperature will induce magnons of differing energy and polarisation (if antiferromagnetic), as random fluctuations in the temperature exist. Using an oscillating magnetic field, with a given frequency, will on the other hand induce coherent spin waves. The difference in these two methods will be illustrated in simulations.

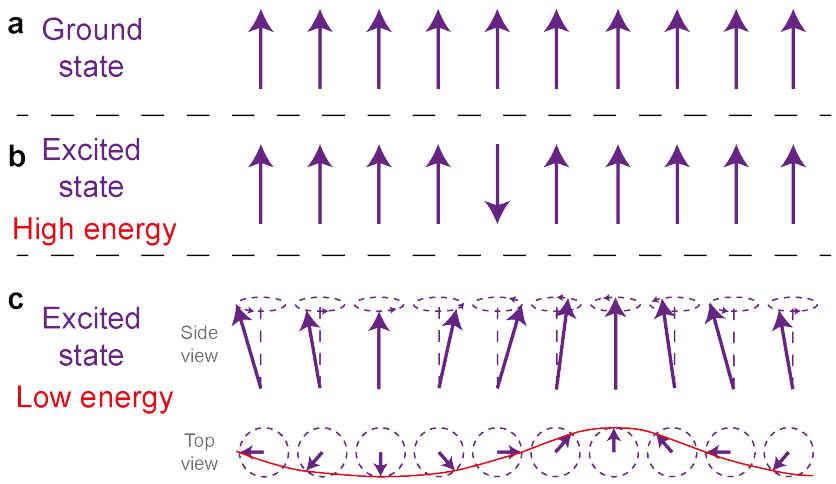

Figure 3.2: Spin wave illustrated in a uniform ferromagnet (c), as compared with the ground state (a) and a state in which one spin is flipped. This figure is reproduced from [26].

Chapter 4

Micromagnetic simulations

Numerical simulations is an important tool when considering large spin systems, as analytical solutions are not always possible. Two types of simluations are commonly used, micromagnetic and atomistic. The basis of these is already given through the mathematical equations introduced for the different spin interations. An illustation of the two is given in figure 4.1.

Micromagnetic simulations are what will be used in this thesis. The models assume a continuous magnetisation vector field $\mathbf{m}(\mathrm{r}, t)$ in predefined *finite difference cells*. One thereby says that, within each cell, the exchange interaction makes all spins perfectly aligned [28]. This is a simplification compared to considering each spin individually. As such, systems in which the magnetisation changes very rapidly in space are inapt for micromagnetic simulations. However, when suitable the model yields obvious advantages in term of simplicity and speed compared to an atomistic one.

One micromagnetic simulation program is mumax3, developed by the DyNaMat group of professor Van Waeyenberge at Ghent University, available as open-source code [29]. It is GPU-accelerated, and made for simluations of ferromagnetic material. Successful simulation of antiferromagnetics in micromagntic simulation models has been claimed by setting a negative value for A, though this is not a mentioned possibility by the creators of the program. The discussion forum on the mmax^3 site also indicates a divided scientific community, as many are sceptical.

Mumax3 utilises Kutte Runga methods for propagating the LLG equation in time. The default method, and the one recommended using for simulations run at 0K, is the Dormand-Prince method (RK45). It has a 5th order converence and a 4th order error estimate. Heun's method is also available, and recommended for use with fixed temperatures.

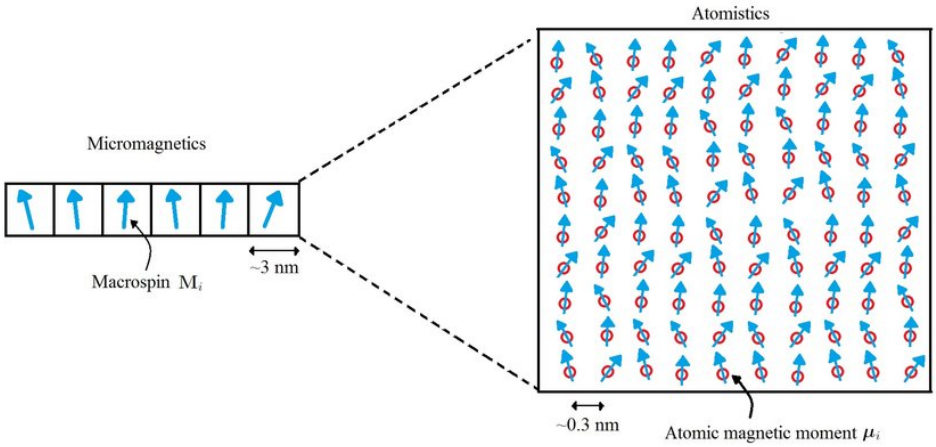

Figure 4.1: The difference between micromagnetics and atomistics, illustrated grapically. In this specific example, the size of the finite cell regions in the micromagnetic approach is set to 3 nm, while the atomic spacing used in the atomistic approach is 0.3 nm. The figure is reproduced from [27].

Part II

Motion of ferromagnetic topological solitons

The aim of the thesis has been mentioned as studying the motion of AFM spin structures. Even so, some time has been spent on looking at the motion of ferromagnetic topological solitons, here domain walls and skyrmions. FMs are more thoroughly understood, and can thus be useful as an introduction to AFMs. This applies to both the theory, and to the numerical models. Furthermore, looking at the FM structures will provide insights into situations in which AFM will be better suited.

As such, this part will look at ferromagnetic domain walls, both in a static case and when an electrical current has been applied. Towards the end of this part of the thesis, FM skyrmions will be simulated micromagnetically. As a skyrmion consists of a circular domain wall, the theory from the ferromagnetic domain walls will still be relevant, though most likely insufficient to describe the skyrmion motion.

Considering the simulations done, it can generally be assumed that any parameter not explicitly mentioned when comparing simulations has been keep constant. Furthermore it should be noted that in all the following simulations, either a domain wall or a skyrmion is set as the initial configuration of the spins. The creation of such magnetic structures has not been considered.

Chapter 5

Static equilibrium state of FM domain wall

5.1 Theoretical predictions

The simplest case of a spin system involving a chiral spin texture is the equilibrium state of a static domain wall, with no externally applied forces. It is therefore suitable as the initial system to consider. The derivations in this chapter will follow work done by Enoksen [30].

Repeating the final result from chapter 2.4, the ferromagnetic LLG equation can be written as

$$\frac{d\mathbf{M}}{dt} = -\gamma \mathbf{M} \times \mathbf{H}_{eff} + \frac{\alpha}{M_S} \mathbf{M} \times \frac{d\mathbf{M}}{dt} + \boldsymbol{\tau}. \tag{5.1}$$

Considering the static case by setting the time derivatives to zero, the equation reduces to

$$\mathbf{M} \times \mathbf{H}_{eff} = 0. \tag{5.2}$$

The potential energy of a system with Heisenberg exchange energy, an easy axis in the z-direction and a hard axis in the y-direction is

$$U = A(\nabla \mathbf{m})^2 + K_h(\mathbf{m} \cdot \hat{\mathbf{y}})^2 - K_e(\mathbf{m} \cdot \hat{\mathbf{z}}))^2, \tag{5.3}$$

where K_h and K_e are the respective uniaxial anisotropy constants, and the DMI has been disregarded. This makes the effective magnetic field

$$\mathbf{H}_{eff} = 2A\nabla^2\mathbf{m} - 2K_h m_y\hat{\mathbf{y}} + 2K_e m_z\hat{\mathbf{z}}. \tag{5.4}$$

Normalised anisotropy fields can be defined as

$$H_\perp = \frac{2K_h}{M_s} \quad \text{and} \quad H_k = \frac{2K_e}{M_s}, \tag{5.5}$$

giving

$$\mathbf{H}_{eff} = \frac{2A}{M_S^2}\nabla^2\mathbf{M} - \frac{H_\perp}{M_s}M_y\hat{\mathbf{y}} + \frac{H_k}{M_s}M_z\hat{\mathbf{z}}. \tag{5.6}$$

Looking at the case of a 1D domain wall, a useful parameterisation is

$$\mathbf{m}(x,t) = [\,\sin\theta\cos\phi\,,\ \sin\theta\sin\phi\,,\ \sigma\cos\theta\,], \tag{5.7}$$

with $\mathbf{m} = \mathbf{M}/M_s$ being the magnetisation direction. $\theta = \theta(x)$ is the angle between the local magnetisation $\mathbf{m}$ and the easy axis, while $\phi = \phi(t)$ is a measure of the deformation of the domain wall, referred to as the tilt angle. Equation 5.2, looking at one spatial component at the time and using the given parameterisation, then becomes

$$\begin{aligned} 0 &= \frac{2A}{M_s^2}\frac{\partial^2}{\partial x^2}\big(\sin\theta\cos\phi\big) \\ 0 &= \frac{2A}{M_s^2}\frac{\partial^2\sin\theta}{\partial x^2}\cos\phi, \end{aligned} \tag{5.8}$$

$$\begin{aligned} 0 &= \frac{2A}{M_s^2}\frac{\partial^2}{\partial x^2}\big(\sin\theta\sin\phi\big) - \frac{H_\perp}{M_s}\sin\theta\sin\phi \\ 0 &= \Big[\frac{2A}{M_s^2}\frac{\partial^2\sin\theta}{\partial x^2} - \frac{H_\perp}{M_s}\sin\theta\Big]\sin\phi, \end{aligned} \tag{5.9}$$

$$\begin{aligned} 0 &= \frac{2A}{M_s^2}\frac{\partial^2}{\partial x^2}\big(\sigma\cos\theta\big) + \frac{H_k}{M_s}\sigma\cos\theta \\ 0 &= \frac{2A}{M_s^2}\frac{\partial^2\cos\theta}{\partial x^2} + \frac{H_k}{M_s}\cos\theta. \end{aligned} \tag{5.10}$$

One solution to the above equations occur when no deformation of the domain wall takes place ($\phi = 0$). While this makes equation 5.9 trivial, the other two equation can be combined to give

$$\Big(\frac{\partial^2 \sin\theta}{\partial x^2}\Big)\cos\theta - \Big(\frac{\partial \cos\theta}{\partial x^2}\Big)\sin\theta = \frac{M_s H_k}{2A}\sin\theta\cos\theta \tag{5.11}$$

Defining a characteristic length as $\lambda = (2A/M_s H_k)$, the second solution can be rewritten to

$$\begin{aligned}
\Big(-\sin\theta\big(\frac{d\theta}{dx}\big)^2 + \cos\theta\frac{d^2\theta}{dx^2}\Big)\cos\theta + \Big(\cos\theta\big(\frac{d\theta}{dx}\big)^2 + \sin\theta\frac{d^2\theta}{dx^2}\Big)\sin\theta &= \frac{\sin\theta\cos\theta}{\lambda^2} \\
\frac{d^2\theta}{dx^2}\Big(\cos^2\theta + \sin^2\theta\Big) &= \frac{\sin\theta\cos\theta}{\lambda^2} \\
\frac{d^2\theta}{dx^2} &= \frac{\sin\theta\cos\theta}{\lambda^2}.
\end{aligned} \tag{5.12}$$

Integrating over x once gives

$$\begin{aligned}
\int \frac{d^2\theta}{dx^2}\frac{d\theta}{dx}dx &= \int \frac{\sin\theta\cos\theta}{\lambda^2}\frac{d\theta}{dx}dx \\
\Big(\frac{d\theta}{dx}\Big)^2 &= \frac{\sin^2\theta}{\lambda^2} + C.
\end{aligned} \tag{5.13}$$

Considering the one-dimensional domain wall, it is defined that $\theta(x) \longrightarrow \pm 1$ as $x \longrightarrow \pm\infty$. As one considers a region infinitely far from the domain wall, all spins will be strictly parallel or antiparallel to the easy axis. Consequently it is known that $\sin\theta \longrightarrow 0$ as $x \longrightarrow \pm\infty$, and the integration constant disappears. Taking the root of the equation, one gets

$$\begin{aligned}
\frac{d\theta}{dx} &= \frac{\sin\theta}{\lambda} \\
dx &= \frac{\lambda}{\sin\theta}d\theta.
\end{aligned} \tag{5.14}$$

Integrating over x on both sides gives

$$\begin{aligned}
x + C &= \lambda\ln\big(\tan(\theta/2)\big) \\
e^{\frac{x+C}{\lambda}} &= \tan(\theta/2),
\end{aligned} \tag{5.15}$$

where C again is an undetermined integration constant. Using the trigonometric identities

$$\cos\theta = \frac{\tan^2(\theta/2) - 1}{\tan^2(\theta/2) + 1} \quad \text{and} \quad \sin\theta = \frac{2\tan(\theta/2)}{1 + \tan^2(\theta/2)}, \tag{5.16}$$

one gets

$$\begin{aligned} \cos\theta &= \frac{e^{\frac{2(x+C)}{\lambda}} - 1}{e^{\frac{2(x+C)}{\lambda}} + 1} \quad \text{and} \quad \sin\theta = \frac{2e^{\frac{(x+C)}{\lambda}}}{1 + e^{\frac{2(x+C)}{\lambda}}} \\ \cos\theta &= \frac{e^{\frac{(x+C)}{\lambda}} - e^{\frac{-(x+C)}{\lambda}}}{e^{\frac{(x+C)}{\lambda}} + e^{\frac{-(x+C)}{\lambda}}} \quad \text{and} \quad \sin\theta = \frac{2}{e^{\frac{(x+C)}{\lambda}} + e^{\frac{-(x+C)}{\lambda}}} \\ \cos\theta &= \tanh\left(\frac{x+C}{\lambda}\right) \quad \text{and} \quad \sin\theta = \operatorname{sech}\left(\frac{x+C}{\lambda}\right). \end{aligned} \tag{5.17}$$

The integration constant is chosen as the position of the domain wall, X, making the final relations

$$\cos\theta = \tanh\left(\frac{x-X}{\lambda}\right) \quad \text{and} \quad \sin\theta = \operatorname{sech}\left(\frac{x-X}{\lambda}\right). \tag{5.18}$$

The definition of λ can now be seen to be a measure of the domain wall thickness.

5.2 Simulations

Micromagnetic simulations were run in mumax3, all initialised with a 180° Néel DW and with equal exchange stiffnesses. The anisotropy, when included, was uniaxial with the easy axis being in the x direction. No hard axis was implemented, and the results here should thus not be exactly equal to the theoretical predictions. The simulations were run using the built in mumax3 function for minimising free energy of a system, with cell sizes of 1 angstrom and only one cell layer included in the z-dimension. The results of differing strengths of DMI and anisotropy are shown in figure 5.1.

The first row of figure 5.1 shows the relaxed states of the domain wall with differing strengths of the anisotropy constant, while the strength of the DMI is set to zero. The effects shown are thus only due to the changes in the exchange stiffness to anisotropy strength ratio. It can be seen that increasing the strength of the anisotropy while keeping the exchange strength constant decreases the domain wall width, as was predicted. It can in figure 5.1 d) to f) further be seen that a higher DMI constant favours a higher volume fraction of domain wall to uniform configuration by both increasing the width of the DW and altering its shape, also keeping in accordance with theory.

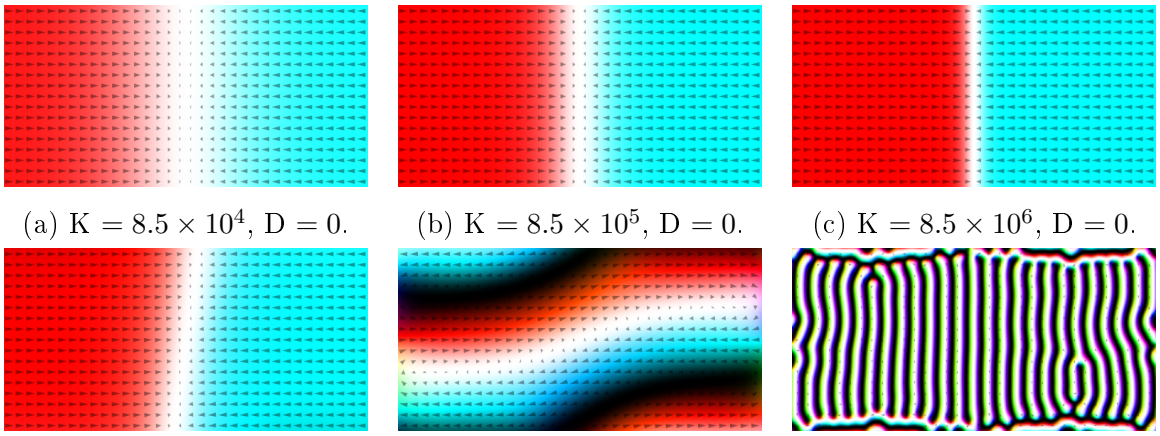

(a) K $= 8.5 \times 10^4$, D $= 0$.

(b) K $= 8.5 \times 10^5$, D $= 0$.

(c) K $= 8.5 \times 10^6$, D $= 0$.

(d) K$= 8.5 \times 10^5$, D$= 5.5 \times 10^{-4}$.

(e) K$= 8.5 \times 10^5$, D$= 5.5 \times 10^{-3}$.

(f) K$= 8.5 \times 10^5$, D$= 5.5 \times 10^{-2}$.

Figure 5.1: Relaxed spin configurations of a ferromagnetic domain wall, with differing DMI and anisotropy strengths. The easy axis is aligned along the x axis. The local magnetisation is represented both in arrows and colour. Red and blue indicate spin directions along the x axis, green and yellow along the y axis, white and black regions along the z axis.

Chapter 6

Current-induced spin-transfer torque on FM domain walls

6.1 Theoretical predictions

Electrical currents have been found to be efficient in moving magnetic textures [14]. When a current is introduced into a magnetic material, the conservation of angular momentum combined with the exchange interaction will cause the direction of the spins in both the introduced electrons and localised spins of the material to alter. This was formulated quantitatively by Berger in 1970 [19], introducing the spin-transfer torques as written in equations 6.1 and 6.2. The former equation considers the adiabatic Berger spin-transfer torque, and the latter the non-adiabatic Berger spin-transfer torque.

$$\boldsymbol{\tau}_B(\mathbf{r}) = \frac{\gamma\hbar}{2eM_s} P(\mathbf{j}\cdot\nabla)\mathbf{m} \tag{6.1}$$

$$\boldsymbol{\tau}_{B\beta}(\mathbf{r}) = \frac{\gamma\hbar}{2eM_s} \beta P\mathbf{m}\times(\mathbf{j}\cdot\nabla)\mathbf{m} \tag{6.2}$$

Here P is the spin polarisation of the current, $\mathbf{j}$ is the electric current density and β is the non-adiabaticity parameter. Comparing the form of equations 6.1 and 6.2 to that of the LLG, it appears that the adiabatic equation induces progression-like motion while the non-adiabatic equation has a damping-like form. β is hence similar to the α previously discussed in that is can take values between 0 and 1, giving the degree of damping. Looking at an electrical current in the positive x-direction, the equations simplify to

$$\boldsymbol{\tau}_B(\mathbf{r}) = \frac{\gamma\hbar}{2eM_s} P j_0 \frac{d\mathbf{m}}{dx} = v\frac{d\mathbf{m}}{dx} \tag{6.3}$$

$$\boldsymbol{\tau}_{B\beta}(\mathbf{r}) = \frac{\gamma\hbar}{2eM_s} \beta P j_0 \mathbf{m}\times\frac{d\mathbf{m}}{dx}, \tag{6.4}$$

having defined $v = \gamma\hbar P j_0/2eM_s$ as a magnitude of the spin transfer torque. Using the Berger spin-transfer torques as the additional forces in equation 2.19, and the parameterisation of $\mathbf{m}$ as given in equation 5.7 with the steady state conditions (considering the domain wall position X and the tilt angle ϕ as functions of time), a relation between the tilt angle and the domain wall position can be found for each of the components. Integrating this with regard to x, with limits set to $\pm\infty$, the relations simplifies into

$$-v\sigma + \frac{K_2\gamma\lambda}{2}\sin(2\phi) - \alpha\lambda\partial_t\phi = \sigma\partial_t X \tag{6.5}$$

$$v\beta\sigma + \alpha\sigma\frac{\partial X}{\partial t} = \lambda\frac{\partial\phi}{\partial t}. \tag{6.6}$$

Combining these equations, as well as introducing dimensionless parameters, gives

$$\sigma(1+\alpha^2)\dot{\tilde{X}} = \sin(2\phi) - \sigma(1+\alpha\beta)\tilde{v} \tag{6.7}$$

$$(1+\alpha^2)\dot{\tilde{\phi}} = \alpha\sin(2\phi) - \sigma(\alpha-\beta)\tilde{v}. \tag{6.8}$$

The dimensionless parameters are here defined as $\dot{\tilde{X}} = \partial(X/\lambda)\,\partial\tilde{t}$, $\dot{\tilde{\phi}} = \partial\phi/\partial\tilde{t}$, $\tilde{t} = (\gamma H_\perp/2)t$, $\tilde{v} = (2/\gamma\lambda H_\perp)v$.

It's been mentioned that the tilt angle refers to the deformation of the domain wall. The process of domain wall deformation occurring when $\dot{\phi} \neq 0$ is known as *Walker breakdown*. A deformed domain wall will no longer be able to contain information, making Walker breakdown something to be avoided and imposing a constraint on the amount of current which should be applied [30]. However, it can also be seen that the domain wall velocity is proportional to the driving forces through the variable $\tilde{v}$, and an as high as possible transfer rate of information is desirable. To get the most efficient system, one must thus maximise $\dot{X}$ while maintaining a zero $\dot{\phi}$. The Walker breakdown is also highly material dependent through both α and β.

Assuming that a systems avoids Walker breakdown, the above equations yields the domain wall velocity as

$$\dot{\tilde{X}} = -\frac{\beta}{\alpha}\tilde{v} \tag{6.9}$$

6.2 Simulations

Simulations were done in mumax3 at 0 temperature, with a sample of $51.2\times25.6\times0.1$ nm and 0.1 nm cell size. The material parameters were $\beta = 0.15$, $\alpha = 1.0$, $M_{\text{sat}} = 384\times10^3$ A/m, $D_{\text{bulk}} = 0$, $K_{u1} = 8.5\times10^5$ J/m^3 and $K_{u2} = 3\times10^5$ J/m^3. Surface charges were removed at $x = 0$ and $x = 25.6$ nm to mimic an infinitely long wire. A domain wall was initialised equally as in the previous chapter, and an electrical current was

subsequently applied in the x-direction. The domain wall position was measured with a built-in function.

6.3 Results and discussion

The result of several simulations run is shown in figure 6.1 as the average velocity of the domain wall. In the graph it shows that the average velocity of a domain wall generally increases with both β and the applied force. This corresponds to the predictions found. The graph is plotted for a varying polarisation of the electrical current, but all other factors in the $\tilde{v}$-parameter used in the derivations are kept constant.

A further point to notice is that the graphs plotted do not appear linear, as they should have been if no Walker breakdown had been present. The determining of the domain wall position appears to be an average domain wall position in y, and will thus become unaccurate with the onset of Walker breakdown. For better control of the process, a new function should ideally be defined in which the tilt angle is also monitored. A limitation in the results is also the number of runs done, as only eight polarisations were tested. As the onset of Walker breakdown of the domain wall will ruin the information which might be stored in the domain/domain walls in a spintronics application, simulations like this could be practical in determining the value range of the parameters which are optimal. As the speed of the device will depend strongly on the average velocity of the domain wall, an optimal position would be one without any breakdown of the wall, while still maintaining a high velocity.

An illustration of the tilt angle can be seen in figure 6.2. A current is applied perpendicularly to a ferromagnetic domain wall, and the figure shows the spin configuration as time passes. It can be seen, particularly in image c), that the tilt angle here is non-zero.

A further observation to be taken from figure 6.2 is that the colour of the domain wall itself, as well as the directions of the spins close to the domain wall, changes in a cyclic manner in time. White colour indicates spins pointing in a positive z direction, while black colour indicates a negative z direction. The figure therefore shows that the domain wall is spinning.

Spinning domain walls occur whenever the free energy of the domain wall is independent on direction of the spins. Both the Heisenberg exchange interaction and the DMI are nearest-neighbour interactions. The anisotropy interaction, on the other hand, has a preferred alignment across the entire sample, but as that direction is impossible for the domain wall, it will not differentiate between the domain wall directions in this case. An unspinning domain wall is obtained in materials with more than one uniaxial anisotropy, as was the case in the analytical derivation.

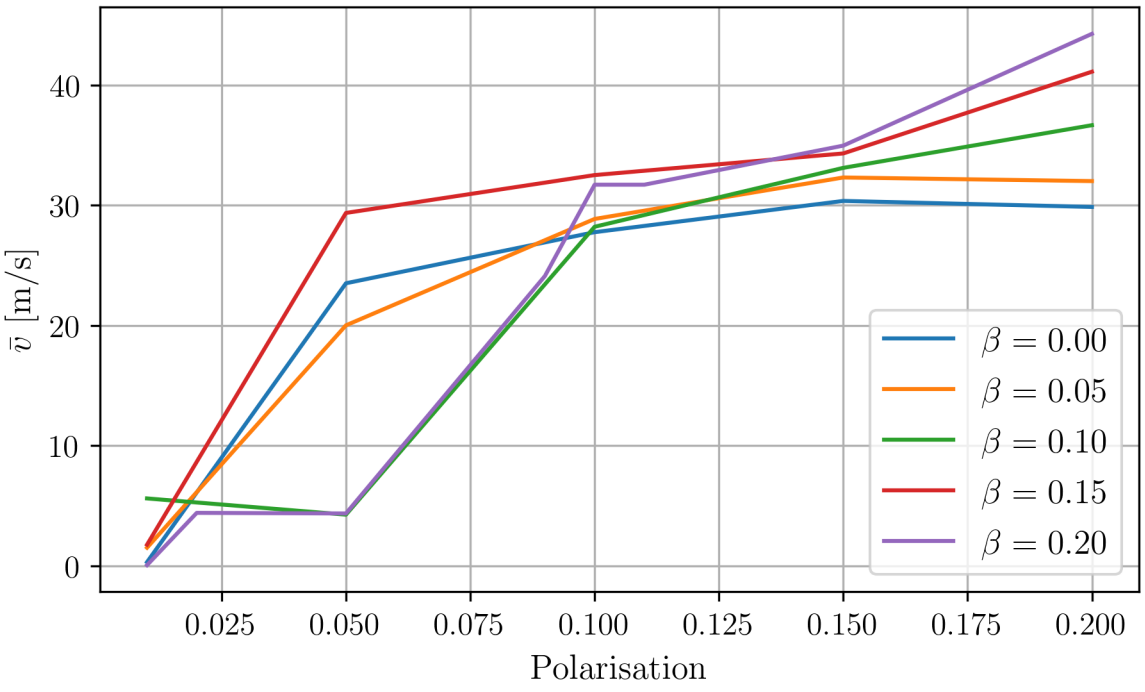

Figure 6.1: Average velocity of domain walls exposed to an electrical current, as a function of the of the polarisation of the current. All other aspects of the simulations were identical, with the current density being 1.5×10^{13} A m^{-2}.

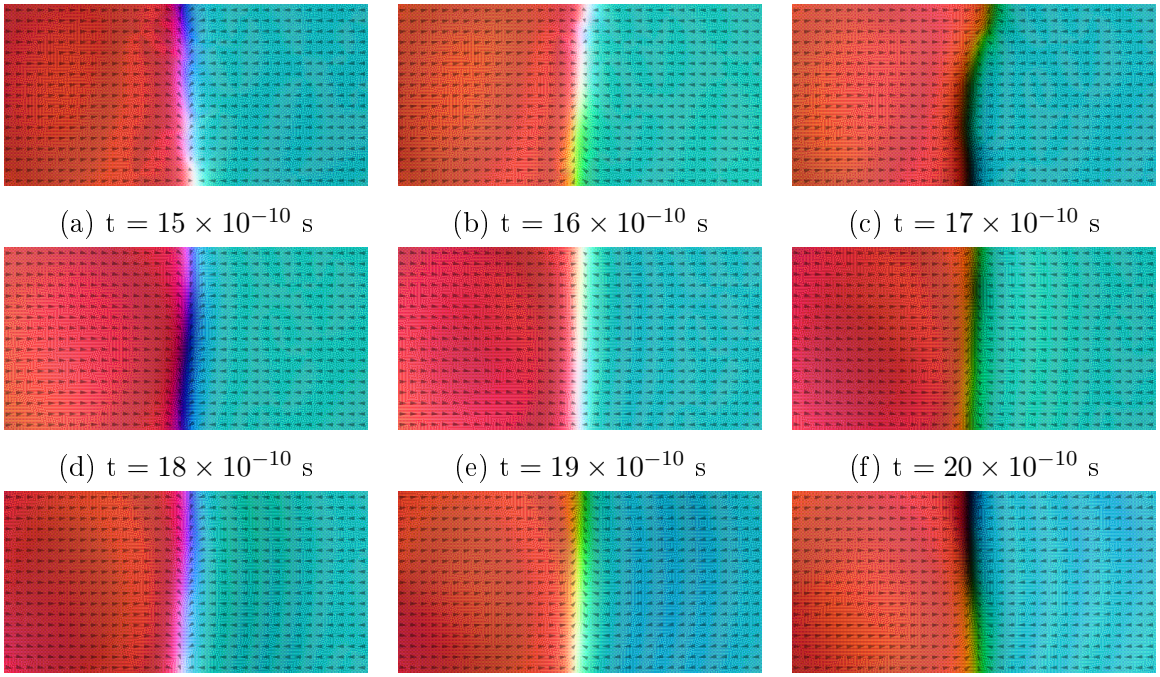

(a) t = 15×10^{-10} s (b) t = 16×10^{-10} s (c) t = 17×10^{-10} s

(d) t = 18×10^{-10} s (e) t = 19×10^{-10} s (f) t = 20×10^{-10} s

(g) t = 21×10^{-10} s (h) t = 22×10^{-10} s (i) t = 23×10^{-10} s

Figure 6.2: Images showing of the effect of an applied electrical current on a ferromagnetic domain wall from a micromagnetic simulation. The domain wall is kept centered in the frame. The system here only has one uniaxial anisotropy, an easy axis aligned in the same direction as the applied current.

Chapter 7

Ferromagnetic skyrmions

Ferromagnetic skyrmions, consisting of a circular ferromagnetic domain wall, should intuitively be dependent on many of the same factors as the domain walls. Simulations were run in which the effect of altering the relative strengths of the different material parameters on ferromagnetic skyrmions are seen, as well as the motion of the skrymion when applying an electrical current.

7.1 Simulations

Mumax3 offers the option of setting a Néel or Bloch skyrmion as the initial spin configuration, which was used for all the simulations done in this section. The size of the initial skyrmion can be altered with a scaling factor, without any more spesifications of the function being given [29]. The material properties were based on a paper considering a thin film of Co on a Pt-substrate [31], and were set as $M_s = 580 \times 10^3$ A/m, $A = 15 \times 10^{-12}$ J/m, $K_{u1} = 0.8 \times 10^6$ J/m^3, $\alpha = 0.3$, and the DMI constant varying between 0 and 9×10^{-3} J/m^2.

7.2 Results and discussion

From the theory, it is known that the width of the skyrmion is proportional to the DMI parameter strength, and that the radius of the inner domain should be dependent in some more complicated manner. Figures 7.1 and 7.2 confirm the dependece on the DMI constant. It can further be seen that there is a minimum value of D for which the skyrmions will be stable for the different initial conditions, as one condition in figure 7.1 and two in figure 7.2 show a purely ferromagnetic sample upon relaxation. The sizes of the skyrmions in the given figures can also be noted to be limited in size by the sample size, as the skyrmions can be seen to adopt a square-like shape.

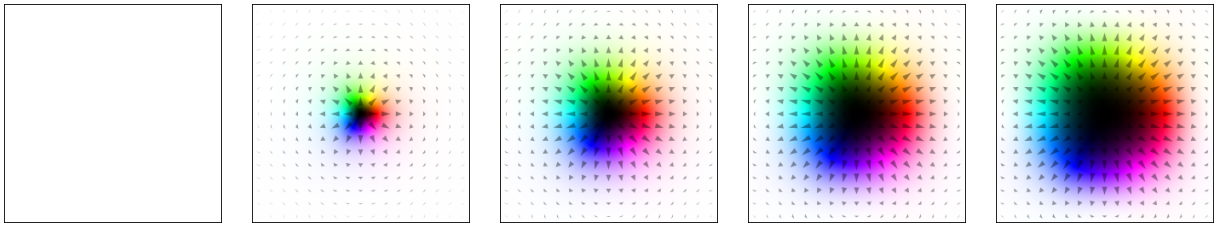

(a) D = 1.0×10^{-3} (b) D = 2.0×10^{-3} (c) D = 3.0×10^{-3} (d) D = 4.0×10^{-3} (e) D = 5.0×10^{-3}

Figure 7.1: Stable Néel skyrmions found in mumax3 with differing strengths of the interfacial DMI parameter. The initial configuration was here a skyrmion, scaled with a factor 3.

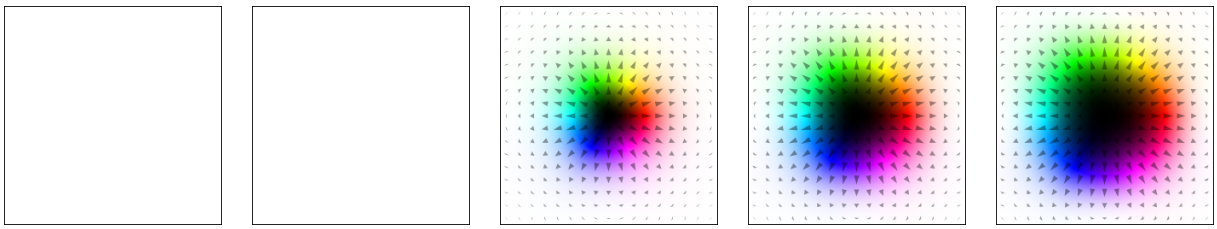

(a) D = 1.0×10^{-3} (b) D = 2.0×10^{-3} (c) D = 3.0×10^{-3} (d) D = 4.0×10^{-3} (e) D = 5.0×10^{-3}

Figure 7.2: Stable Néel skyrmions found in mumax3 with differing strengths of the interfacial DMI parameter. The initial configuration was here a skyrmion, scaled with a factor 1.

Simulations were done in which the value of the damping parameter α was varied. Though unrealistic in a real material, the value $\alpha = 1.0$ was found easiest detectable. As such, a α-value of 1.0 was used for the results presented in figures 7.3 and 7.4. In 7.3, the aim of the simulation was to gain some insight as to how fast skyrmions move with respect to varying material parameters. From the results it can be seen that the relation is not as simple as with domain walls, if it does exist. The average velocity in the direction of the applied electric current, varies greatly both in size and in sign.

It should further be noted that the skyrmions also move significantly in the y direction, i.e. perpendicular to the applied electric current. Referring to the topological Hall effect, this is as expected.

The greatly varying average velocities in both x and y calls for more research, both theoretical and numerical. However, one possibility is that the fault stems from the numerical simulation, giving incorrect results. This is especially suspected from the results found in 7.4, as decreasing the size of time steps of a numerical method should normally give either the same result, or a more accurate one. Here the two simulations show completely different movements of the skyrmion, both in direction and velocity. However, the simulations have here used the Heun method at zero temperature, though it was later found that this is not recommended [29]. Unfortunately there was not sufficient time to rerun the simulations with a different method.

A more accurate and reliable measurement of the skyrmion positions should also be implemented, as the measuring for figure 7.4 was done manually in InkScape. This has also put a restriction on the amount of data which could be measured.

With the uncertain results shown, no conclution can be drawn regarding the movement of the skyrmion, other than that motion does in fact occur when an electrical currect is applied to the material. Also, the formation and stability of the ferromagnetic skyrmion seems to correspond with the theoretical trends found.

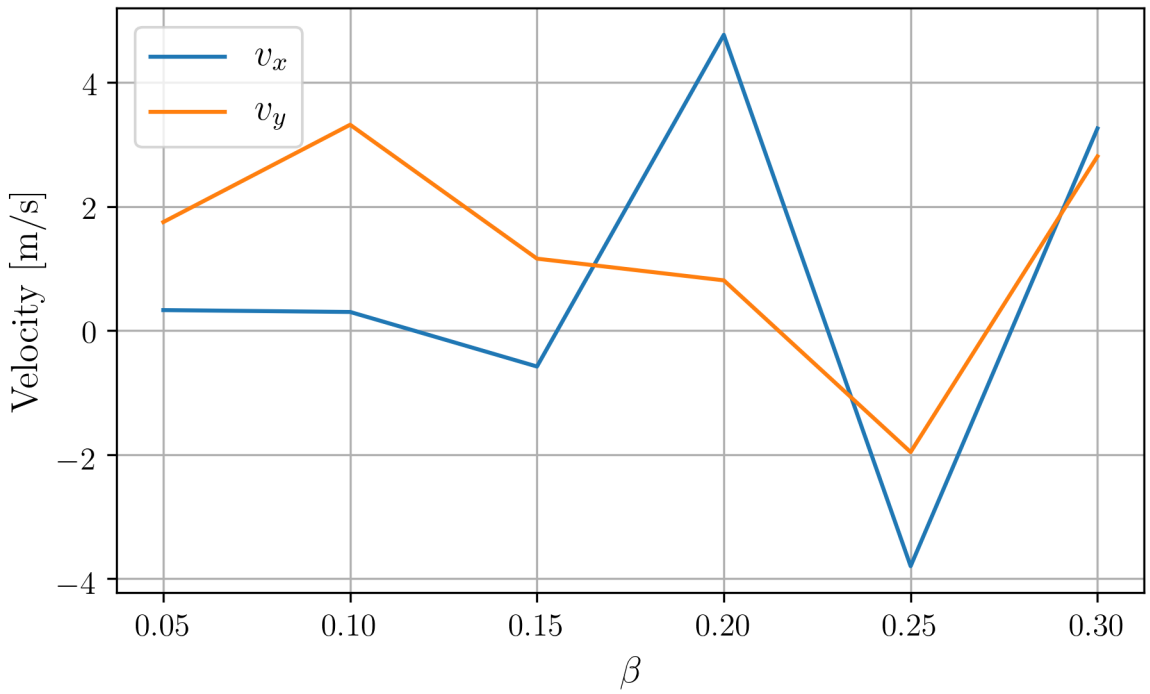

Figure 7.3: The average skyrmion velocities as a function of the non-adiabaticity parameter, β. The velocity in x is parallel to the applied electrical current, while the velocity in y is perpendicular to it. The average velocities where found from 2×10^{-9} second simulations. The polarisation of the spin current applied was 0.01.

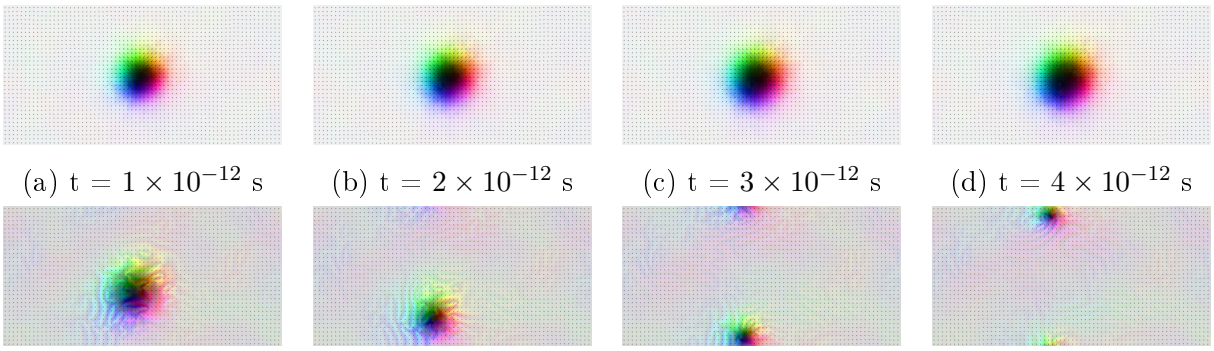

(a) t = 1×10^{-12} s (b) t = 2×10^{-12} s (c) t = 3×10^{-12} s (d) t = 4×10^{-12} s

(e) t = 1×10^{-12} s (f) t = 2×10^{-12} s (g) t = 3×10^{-12} s (h) t = 4×10^{-12} s

Figure 7.4: The motion of a ferromagnetic skyrmion shown through snapshots from the simulation. An electrical current applied in the x direction. The difference between the upper and lower row of images lies in the time steps used in the Heun method in mumax3, respectively 1×10^{-14} and 1×10^{-15} seconds. Periodic boundary conditions were used in the simulation.

Part III

Motion of antiferromagnetic skyrmions

It's been mentioned that antiferromagnetic materials can provide higher switching frequencies than ferromagnetic materials. This part of the thesis will therefore look at the motion of magnetic structures in antiferromagnetic materials, specifically at antiferromagnetic skyrmions. Furthermore, while the previous part considered applied electrical currents and thus motion which takes place in conducting materials, a motivation for this thesis was to consider systems in which information is transmitted without the electrons themselves moving. As such, the focus will be shifted to insulating materials, and therefore the focus will also be shifted from interactions involving electrical currents to interactions involving spin waves.

Spin waves can be created in several manners, and the method chosed will affect the properties of the wave. This chapter will look at both applying a temperature gradient and a localised magnetic field as methods for creating spin waves, and the subsequent motion of a skyrmion experiencing the spin waves.

Chapter 8

Motion of AFM skyrmions by temperature gradient

At zero temperature, the characteristics of magnetic materials are deterministic. This is in contrast to looking at systems at finite temperature, in which case one will be dealing with random thermal fluctuations, and will as such have to involve theory from statistical thermodynamcis. It being assumed that the temperature never exceeds the Néel temperature, the material will still be ordered. The higher energy state can then manifest itself through spin waves, as demonstrated in figure 3.2. This chapter will look at the effects of thermally induced spin waves on antiferromagnetic skyrmions, both analytically and through simulations.

A prerequisite to this work is that temperature gradients generate a flux of magnons, as found by Gomonay et. al. [32], where the magnons were found to either reflect off or be absorbed into the AFM skyrmion. Which of these occurred depended on a multitude of factors, such as the size of the skyrmion, and the energy and polarisation of the magnons. Furthermore, a recent study by Koshlahni et. al. [33] of antiferromagnetic skyrmions in a temperature gradient found that the skyrmions move with a topological Hall angle of zero, and with the magnitude of the motion being particularly dependent on the damping of the system, and the size of the skyrmions. The simulation method used in that paper was atomistic, so doing a micromagnetic one here should reproduce equivalent results. Also, the article contains analytical calculations of the skyrmion motion, which will be reproduced in section 8.1. The paper written by Koshlahni et. al. should be considered a reference throughout that entire section.

8.1 Theoretical predictions

To describe the motion of an antiferromagnetic skyrmion in a temperature field, the AFM Lagrangian in the continuum limit will be considered, with terms

$$\mathcal{T} = \int d^2\mathbf{r} \frac{1}{2a}\dot{\mathbf{n}}^2, \tag{8.1}$$

$$\mathcal{U} = \int d^2\mathbf{r} \big(\frac{A}{2}(\nabla\mathbf{n})^2 + \frac{D}{d}\mathbf{n}\cdot(\nabla\times\mathbf{n})\big), \tag{8.2}$$

$$\mathcal{R} = \frac{\mu_s\alpha}{\gamma}\int d^2\mathbf{r}\frac{\dot{\mathbf{n}}}{2}, \tag{8.3}$$

where a and A are the homogeneous and inhomogeneous Heisenberg exchange coefficients, D is the inhomogeneous Dzyaloshinskii-Moriya coefficient and d is the atomic spacing. Working in the continuum limit it will be assumed that d is much smaller than the size of the magnetic structures. Following the same precedure as when finding the LLG equation, the Euler-Lagrange equations give the relation as

$$\frac{1}{a}\ddot{\mathbf{n}} - \frac{\delta\mathcal{U}}{\delta\mathbf{n}} + \frac{\mu_s\alpha}{\gamma}\dot{\mathbf{n}} + 2\lambda\mathbf{n} = 0, \tag{8.4}$$

with a Lagrange multiplier included to ensure that the length of the staggered order parameter is one. As before, crossing with $\mathbf{n}$ from the left gives

$$\mathbf{n}\times\big[\ddot{\mathbf{n}} - a\mathbf{f}_\mathbf{n} + \frac{\mu_s\alpha a}{\gamma}\dot{\mathbf{n}}\big] = 0, \tag{8.5}$$

where $\mathbf{f}_\mathbf{n} = -\delta\mathcal{U}/\delta\mathbf{n}$ is the effective field as caused by the potential energy in the spin interactions.

8.1.1 The Fluctuation-Dissipation Theorem

In statistical mechanics, systems at equilibrium at finite temperature continuously experience thermal fluctuations. The fluctuation-dissipation theorem states that the magnitude of the fluctuations at equilibrium are related to the rate at which the system approaches equilibrium [34]. This can be incoorporated into our model through Langevin dynamics, including temperaure effects by adding a stochastic noise term $\mathbf{f^{th}}$, which takes the shape of a Gaussian field. This gives us the stochastic LLG equation

$$\mathbf{n}\times\big[\ddot{\mathbf{n}} - a(\mathbf{f}_\mathbf{n} + \mathbf{f^{th}}) + \frac{\mu_s\alpha a}{\gamma}\dot{\mathbf{n}}\big] = 0, \tag{8.6}$$

where the mean value of the fluctuation is zero, and the variance is tied to the temperature and the damping constants. In statistical mechanics, this is formulated as

$$\langle f_i^{th}(\mathbf{r},t) f_j^{th}(\mathbf{r}',t')\rangle = 2\xi\delta_{ij}\delta(\mathbf{r}-\mathbf{r}')\delta(t-t'), \tag{8.7}$$

$$\langle \mathbf{f}^{th}(\mathbf{r},t)\rangle = 0, \tag{8.8}$$

where $\xi = \alpha k_B T(x)$ is the mentioned correlation. The temperature is assumed to vary only in x.

As previously mentioned, a spin wave is observable as a fast oscillating motion of the individual spins. This can be described mathematically as

$$\mathbf{n} = \sqrt{1-\delta\mathbf{n}^2}\mathbf{n}^{(0)} + \delta\mathbf{n}, \tag{8.9}$$

where $\delta\mathbf{n}$ is the oscillating component, and $\mathbf{n}^{(0)}$ is the slowly varying magnetic texture. Both are functions of time and space, and are defined such as to give $\delta\mathbf{n}\cdot\mathbf{n}^{(0)} = 0$, and $\langle(\delta\mathbf{n})^{2l+1}\rangle = 0$. In this thesis, expectancy values for any fast oscillating components to an even power higher than 2 have been treated as negligible. Also, as the size of the fluctuation is small, the simplification $(1-\langle\delta\mathbf{n}^2\rangle) \approx 1$ has been used. Looking at equation 8.6 averaged over time with 8.9 inserted then gives

$$\mathbf{n}^{(0)} \times \left[\ddot{\mathbf{n}}^{(0)} - a\mathbf{f}^{th} + \frac{\mu_s}{\gamma} a\alpha\dot{\mathbf{n}}^{(0)}\right] + \boldsymbol{\tau}^{\text{magn}} = 0, \tag{8.10}$$

with the torque created by the thermic energy being

$$\begin{aligned}\boldsymbol{\tau}^{\text{magn}} &= -aA\big(\langle\delta\mathbf{n}\times\partial_i^2\delta\mathbf{n}\rangle - \partial_i\langle\delta\mathbf{n}^2\rangle\mathbf{n}^{(0)}\times\partial\mathbf{n}^{(0)}\big),\\ &= -a\hbar\mathbf{J}^n\cdot\nabla\mathbf{n}^{(0)} + aA(\partial_i\rho)\mathbf{n}^{(0)}\times\partial_i\mathbf{n}^{(0)}.\end{aligned} \tag{8.11}$$

The subscripts in the partial derivative here represent the Einstein notation, and as such represent a sum over $i \in 1,2,3$ as the spatial dimensions. The thermomagnonic torque is rewritten with $J_i^n = (A/\hbar)\mathbf{n}^{(0)}\cdot\langle\delta\mathbf{n}\times\partial_i\delta\mathbf{n}\rangle$ as the current of angular momentum carried by the spin wave and $\rho = \langle\delta\mathbf{n}^2\rangle/2$ as the magnon number density. The two terms of the torque which become apparent, one positive and one negative, are known as the *reactive torque* and the *dissipative torque*, respectively.

8.1.2 Thiele's equation

Equation 8.10 describe the motion of a general staggered order parameter, while the objective in this derivation is to look specifically at the motion of a skyrmion. Following Thiele's approach of collective coordinates [35, 36], and letting the position of the skyrmion centre be $\mathbf{u}(t)$, the staggered order parameter can be written as

$$\mathbf{n}^{(0)}(\mathbf{r},t) = \mathbf{n}^{(0)}\big(\mathbf{r} - \mathbf{u}(t), t\big). \tag{8.12}$$

Multiplying equation 8.10 with $(\mathbf{n}^{(0)} \cdot \partial_i \mathbf{n}^{(0)}\times)$, and using $\dot{\mathbf{n}} = \dot{u}_j \partial_j \mathbf{n}$ and $\ddot{\mathbf{n}} = -\ddot{u}_j \partial_j \mathbf{n} + \dot{u}_j \dot{u}_k \partial_j \partial_k \mathbf{n}$, one obtains the relation

$$\begin{aligned} -\ddot{u}_j(\partial_i \mathbf{n}^{(0)} \cdot \partial_j \mathbf{n}^{(0)}) + \dot{u}_j \dot{u}_k (\partial_i \mathbf{n}^{(0)} \cdot \partial_j \partial_k \mathbf{n}^{(0)}) - a(\partial_i \mathbf{n}^{(0)} \cdot \mathbf{f}^{th}) \\ - a\hbar J_j^n \mathbf{n}^{(0)} \cdot \partial_i \mathbf{n}^{(0)} \times \partial_j \mathbf{n}^{(0)} + aA(\partial_j \rho)\partial_j \mathbf{n}^{(0)} \cdot \partial_i \mathbf{n}^{(0)} = 0, \end{aligned} \tag{8.13}$$

where the constraints $|\mathbf{n}^{(0)}| = 1$ and $\partial^2 \mathbf{n}^{(0)} = 0$ have been used. Integrating this over space, the result is the stochastic Thiele's equation for AFM skyrmions,

$$M^{ij}(\ddot{u}_j + \frac{\mu}{\gamma}\alpha a) + F_i^{th} + F_i^r + F_i^d = 0, \tag{8.14}$$

where one can see that, in addition to the reactive and dissipative terms already found to be present, a thermal one is also included. The terms in the above equation take the forms of

$$F_i^{th}(\mathbf{u},t) = \frac{1}{\Delta^2}\int d^2\mathbf{r}(\partial_i \mathbf{n}^{(0)} \cdot \mathbf{f}^{th}), \tag{8.15}$$

$$F_i^r = \frac{4\pi\hbar Q^n}{\Delta^2}\varepsilon^{ij} J_j^n, \tag{8.16}$$

$$F_i^d = -\frac{c^2}{\Delta^2} M^{ij}\partial_j \rho, \tag{8.17}$$

where $\Delta = d(A/D)$ is a measure of the skyrmion size. The topological number is here defined according to the staggered order parameter

$$Q^n = \frac{1}{4\pi}\int d^2\mathbf{r}\big(\mathbf{n}^{(0)} \cdot (\partial_x \mathbf{n}^{(0)} \times \partial_y \mathbf{n}^{(0)})\big). \tag{8.18}$$

While the topological charge of an antiferromagnetic skyrmion defined by the magnetisation parameter has a net value of 0, being defined by $\mathbf{n}$ it will be more equivalent to the topological of a ferromagnetic skyrmion defined by $\mathbf{m}$, and is here ± 1. The mass tensor in the above equations is given as

$$M^{ij} = \frac{1}{a\Delta^2}\int d^2\mathbf{r}(\partial_i \mathbf{n}^{(0)} \cdot \partial_j \mathbf{n}^{(0)}), \tag{8.19}$$

which is here symmetric and can be simplified to $M^{ij} = M\delta_{ij}$. The effetive AFM magnon velocity in an isotropic material is $c = \sqrt{aA}$. Solving equation 8.14 for the steady state solution, one then obtains the mean velocity of the antiferromagnetic skyrmion as

$$\dot{u}_i = -\frac{\gamma}{Ma\alpha\mu}(F_i^{th} + F_i^r + F_i^d). \tag{8.20}$$

8.1.3 The Fokker-Planck equation

In general terms, the Fokker-Planck equation describes the time evolution of a Brownian particle. It can be combined with the Langevin equation, giving

$$\dot{m}_i = g^{ij}(H_j + h_j^{th}), \tag{8.21}$$

where g_{ij} is a diffusion matrix, $\mathbf{H}$ are deterministic forces and $\mathbf{h}$ are stochastic forces. Considering the probability of finding the skyrmion in position $\mathbf{m}$ at time t to be $P[\mathbf{m}, t]$, the Fokker-Planck equation becomes

$$\partial_t P = -\partial_i(g^{ij}H_j P) + \partial_i\partial_j(\xi g^{ik}g^{jk}P). \tag{8.22}$$

The situation considered assumes a linear temperature gradient in the x-direction, thus giving $\partial_y T = 0$, $\partial_x^2 = 0$, $J_y^m = 0$ and $\partial_y \rho = 0$. The assumption that the magnon current is almost uniform is also done by saying $\partial_x J_x^m = 0$ and $\partial_x^2 \rho = 0$. This gives

$$F_x^r = F_y^d = 0, \tag{8.23}$$

$$F_y^r = -\frac{4\pi\hbar Q^n}{\Delta^2} J_x^n, \tag{8.24}$$

$$F_x^d = -\frac{c^2}{\Delta^2} M\partial_x \rho, \tag{8.25}$$

$$g^{ij} = -\frac{\gamma}{M\alpha a\mu}\delta_{ij}. \tag{8.26}$$

This makes the Fokker-Planck equation for a magnetic soliton

$$\partial_t P = -(gF_x^d - 2g^2\partial_x\tilde{\xi})\partial_x P - gF_y^r\partial_y P + g^2\tilde{\xi}(\partial_x^2 + \partial_y^2)P. \tag{8.27}$$

Looking at only the lowest order terms for AFM skyrmions, the velocity of the skyrmion is given by

$$v_x = gF_x^d - 2g^2\partial_x\frac{aM}{\Delta^2}\xi = \frac{\gamma}{\alpha a\Delta^2\mu}(c^2\partial_x\rho - \frac{2\gamma k_B}{M}\partial_x T) = v_x^n - v_x^B, \tag{8.28}$$

$$v_y = gF_y^r = \frac{4\pi\hbar\gamma Q^n}{M\alpha a\Delta^2\mu} J_x^n = v_y^n, \tag{8.29}$$

where $\mathbf{v}^n$ are the contributions from the thermally induced AFM magnons, and $\mathbf{v}^B$ are the contributions from the Brownian motion.

Considering the motion in the x-direction, both terms have a dependency on $\partial_x T$ through the fact that $\partial_x \rho$ is created by the temperature gradient. The dependencied however have different prefactors, of which the most significant difference is M, the mass of the skyrmion. Through equation 8.19, the mass can be seen, in the case of skyrmions, to more accurately be a measure of the size of the skyrmion. This gives that $\mathbf{v}^n$ is more important for large skyrmions, while the Brownian contribution to the velocity becomes dominant for small skyrmions.

A further interpretation can be found considering $\mathbf{J}^n$, described as the current of spin angular momentum. Looking at the definition of $\mathbf{J}^n$, it can be seen that right-circular and left-circular spin waves carry the same amount of angular momentum - but with opposite signs. Linearly polarised spin waves can be seen not to carry any angular momentum. With the spin waves being induced by random temperature fluctuations, their polarisations will also be random. The mean current of spin angular momentum when considering thermal spin waves is therefore zero. This reduced equation 8.29 to $\mathbf{v_y} = 0$.

8.2 Simulation method

Micromagnetic simulations were done in mumax3, with an antiferromagnetic skyrmion being initialised in the centre of the sample. The method used for the initialisation is described in Appendix A, and the sample was then relaxed to its state of minimal free energy. The sample was $512 \times 128 \times 0.4$ nm large, and had a cell size in x and y of 1 nm. The material parameters used are $A = -15 \times 10^{-12}$ J/m, $M_s = 0.58 \times 10^6$ A/m, $K_u = 0.8 \times 10^6$ J/m^3, $D_{\text{ind}} = 0.0034$ J/m^2 and $\alpha = 0.1$, where the uniaxial anisotropy has an easy axis in the z-direction. The simulations were run for 10 ns each, and temperature gradients of either 0.2, 0.4 or 0.6 K/nm were applied in the x-direction. The temperature at $x = 0$ nm was 0 K, with the temperatures at $x = 512$ nm thus being 102.4 K, 204.8 K and 307.2 K, respectively.

As the simulation is of a stochastic nature, the results which will be presented are the averages over 10 runs. These all had identical intial parameters, with the only difference being their random thermal seedings. No random number generator was found in mumax3, no this was done by generating a random number in Matlab, it here being seeded in time, and manually writing it into the mumax3 input file. A fixed time step of 10^{-15} seconds was used with the Dormand-Prince method [29]. Detecting the location of the skyrmion

was done as described in Appendix B.

8.3 Result and discussion

The main result, the position of the skyrmions as a function of time, is given in figure 8.1. To get a measure of the randomness in the simulation, the average velocity and the standard deviation between the runs are given in table 8.1. It can be seen that two of the temperature gradients, 0.2 and 0.6 K/nm, cause the skyrmion to move toward the warmer side of the sample. The intermediate temperature gradients has the opposite effect, with the skyrmion moving towards the colder side, though at a much slower pace. Simulations were also done with dT = 0.8 K/nm, but often with the result that the skyrmion was deformed. It was therefor not considered in figure 8.1, as a deformed skyrmion would no longer be suited to transfer information.

The average sizes of the skyrmions also appear in the table, and can be seen to increase evenly with increasing temperature.

dT [K/nm]	Diameter [nm]	$\bar{v}_x$ [m/s]	$\bar{v}_y$ [m/s]	SD($\bar{v}_x$) [m/s]	SD($\bar{v}_y$) [m/s]
0.2	14.4	6.6	-1.1	6.3	2.1
0.4	18.8	-2.6	-0.6	9.7	2.0
0.6	23.3	8.9	-0.4	11.0	2.7

Table 8.1: The average AFM skyrmion sizes, velocities and standard deviations of velocity.

The strength of the damping constant affects the rate of decay of the magnons. In the paper by Koshlahni et al. already mentioned [33], a lower damping constant has been used. The velocities obtained there were higher than what is obtained here. Furthermore, the shape of the trajectories are different. Koshlahni et al. found the motion of the skyrmions to be more even, and that the skyrmions, upon reaching the wall of the sample, remained in that area. Such movement could be seen in some individual runs here as well, though not sufficiently often for the behaviour to appear in figure 8.1. However, while Koshlahni et al. have not stated the number of runs their results were averaged over, the number is likely to be higher than 10.

One behaviour taken from equation 8.28 and 8.29 was that large skyrmions tend to move towards the hotter side of the sample, while small skyrmions move towards the colder side [33]. This can be seen not to be a satisfactory explanation, as the intermediate skyrmion in size moved in opposite direction to the two others.

The skyrmions have, as given in table 8.1, not moved significantly in the y-direction. This is in accordance with the discussed theory, indicating that the polarisation of the spin waves obtained are in fact random.

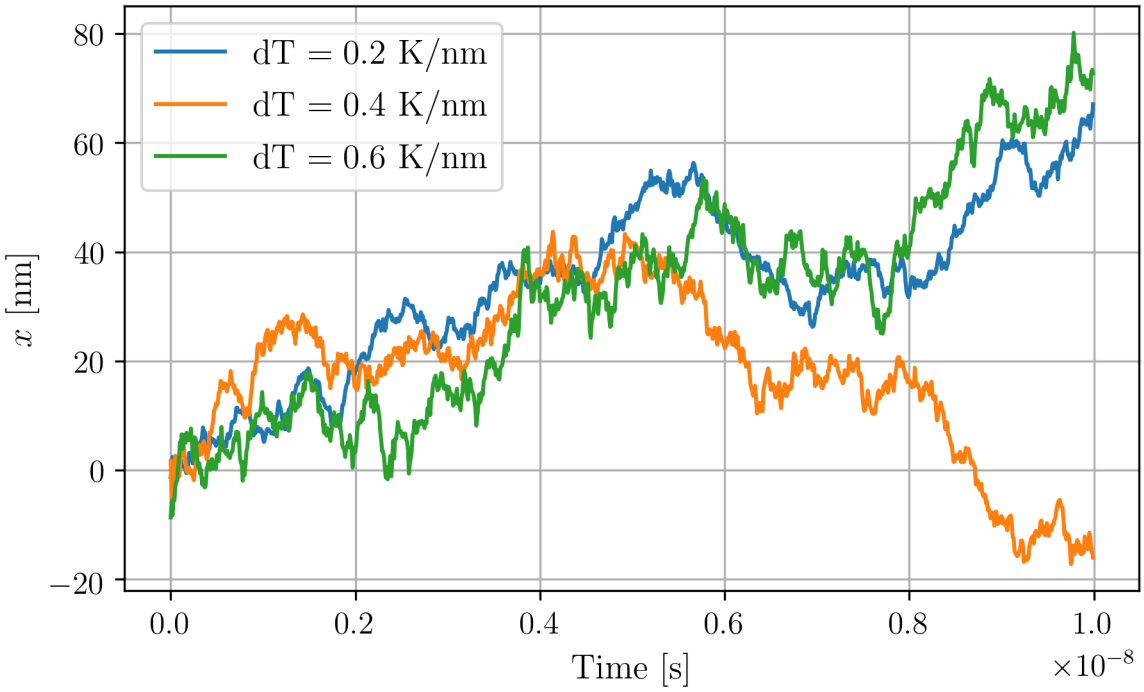

Figure 8.1: The movement of AFM skyrmions in temperature gradients. The gradient is applied in the x-direction, increasing with x. The length of the sample was ± 256 nm. The plotted values are the results of 10 runs, averaged.

One possible source of error in the simulation would be if, in the regions with highest temperatures, the thermal fluctuations were larger than expected. The model on which the mathematical derivation is based assumes that the fluctuations $\delta\mathbf{n}$ can be described as linear. This only holds for situations in which $\sin\theta \approx \theta$. Should the deviation from $\mathbf{n}^{(0)}$ become large, the models used will no longer be valid. An alternative formulation is that the variation in each component of the magnetic moment throughout time should be small. This was checked for by looking at the components of one chosen spin throughout the simulation, as is plotted in figure 8.2. The spin looked at was located close to the right side edge of the sample, thus in the highest temperature. As $\langle m_y \rangle \approx 0.5$, it can be seen that the spin is also influenced by stonger DMI as it is close to the edge.

It is clearly visible that the thermal fluctuations increase with increasing temperature, and the fluctuations also appear much too large for the linear approximation. This holds the consequence of the mathematical description found no longer being suitable. To find the exact discrepancies one would have to repeat the analytical derivation.

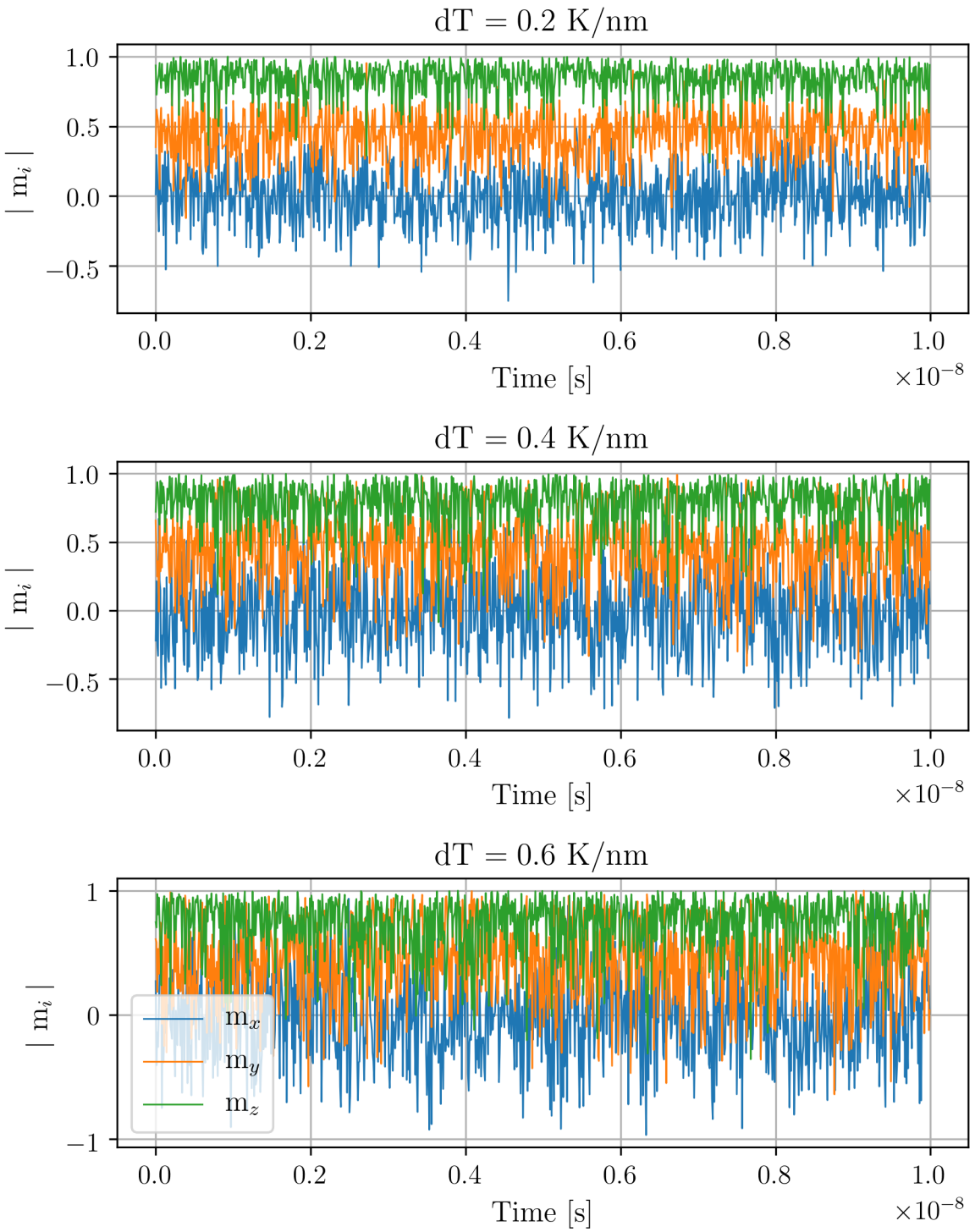

Figure 8.2: Thermal spin fluctuations throughout the length of the simulations (10^{-8} seconds), shown for each of the spatial components. The spin looked at was located close to the hottest region of the sample, and can be seen to be influenced by the DMI in the sample edge in the value of m_y.

Chapter 9

Motion of AFM skyrmions by localised magnetic field

The result of the previous analytical derivation showed that the velocity of skyrmions in a temperature gradient was a competition between Brownian motion and motion induced by spin waves. That result can be adapted for spin waves created by other methods than temperature gradients by setting $\partial_x T = 0$, and thus only considering $\mathbf{n}^n$. One method for generating the magnons is to apply a magnetic field to the sample, but to a region in which the skyrmion itself is not located. This has been done by Ding et. al. [37] for a ferromagnetic system, in which the generated spin waves proved efficient in moving the skyrmion. A requirement is that the frequency of the magnetic fluctuations be close to the spin wave resonance frequency.

Coherent antiferromagnetic spin waves can be either linearly or circularly polarised, both of which can be created using alternating magnetic fields. In [25], Tveten et. al. have found both analytically and through simualtions that antiferromagnetic domain walls experiencing these two types of polarisation will move in opposite directions. If the same behaviour is found with antiferromagnetic skyrmions it would allow a more complex skyrmion control than that found with incoherent spin waves.

9.1 Finding the resonance frequency

The properties of an induced spin wave will, among several factors, be dependent on the oscillating frequency determined by the frequency of the applied magnetic field. This can be expressed through its dispersion relation, in which the relation between the wave vector k and the angular frequency ω is given.

Starting from the LLG equation for a uniform AFM, including Heisenberg exchange and an uniaxial anisoptroy but excluding damping, one has the relation

$$\mathbf{n} \times \left[\ddot{\mathbf{n}} + aA(\nabla^2 \mathbf{n}) + aK(\mathbf{n} \cdot \hat{\mathbf{z}})\hat{\mathbf{z}}\right] = 0. \tag{9.1}$$

The staggered order parameter, describing a spin wave in the x-direction in a uniform AFM, can then be written as

$$\begin{aligned} \mathbf{n}(\mathbf{r}, t) =& \sigma(\mathbf{r})\hat{z} + \delta\mathbf{n}(t) \\ =& \sigma(\mathbf{r})\hat{z} + (\delta n_0^x \hat{x} + \delta n_0^y \hat{y}) e^{i(kx - \omega t)}, \end{aligned} \tag{9.2}$$

in which $\sigma(\mathbf{r}) = \pm 1$, $\delta\mathbf{n}$ is the fast fluctuation of the spin wave taking the form of a travelling wave. Inserting the expression for $\mathbf{n}$ into the LLG then gives

$$\begin{aligned} \mathbf{n} \times \left[\ddot{\mathbf{n}} - a(A\partial_x^2 + \frac{K}{n_z}\hat{z})\right] &= 0 \\ \mathbf{n} \times \left[-\omega^2(\delta n_0^x \hat{x} + \delta n_0^y \hat{y}) e^{-i\omega t} - aKn_z\hat{z}\right] &= 0 \\ \begin{bmatrix} \hat{i} & \hat{j} & \hat{k} \\ \delta n_0^x e^{i(kx-\omega t)} & \delta n_0^y e^{i(kx-\omega t)} & \sigma \\ (-\omega^2 + ak^2)\delta n_0^x e^{i(kx-\omega t)} & (-\omega^2 + ak^2)\delta n_0^y e^{i(kx-\omega t)} & -aK\sigma \end{bmatrix} &= 0, \end{aligned} \tag{9.3}$$

thus giving two non-trivial equations which both take the exact same form. Using dimensional analysis to get an expression with meaningful physical significance, one obtains the dispersion relation

$$\omega = \frac{\sqrt{aK + ak^2}d^2}{\hbar}, \tag{9.4}$$

with d being the atomic spacing. An interesting feature to be noted about the dispersion relation is that is is linear in k. This comes in contrast to ferromagnets, where $\omega \sim k^2$. For the material properties used in mumax3, inserting $k = 0$ to find the resonance frequency gives $\omega_r = 5.288$ THz. In the equivalent ferromagnetic system simulated by Ding et. al., the resonance frequency of the magnons was 85 GHz [37]. This demonstrates that antiferromagnetic systems can provide much faster dynamics than ferromagnetic ones, as has been claimed.

Though the damping normally used in the LLG has been excluded in the above derivation, damping will occur in the system causing the amplitude of the spin wave to decrease as it propagates.

9.2 The predicted skyrmion movement

An assumption made considering the thermal magnons was that the wavelength of the helix be greater than that of the thermal magnons. This allowed simplifications to be done in which terms of higher orders were considered negligible. Considering the velocity of a skyrmion interacting with spin waves at zero temperature can therefore conclusively be said to the exactly equal to $\mathbf{v}^n$ as found in the previous chapter, but are instead given as

$$v_x \approx \frac{\gamma c^2 \partial_x \rho}{\alpha a \Delta^2 \mu}, \tag{9.5}$$

$$v_y \approx \frac{4\pi\hbar\gamma Q^n}{M\alpha a \Delta^2 \mu} J_x^n. \tag{9.6}$$

The coherency of the spin waves is in the skyrmion velocities shown in J_x^n and hence the movement in the y-direction. Considering the value of J_x^n it is expected that right-circular spin waves give $v_y < 0$, left-circular spin waves give $v_y > 0$ and linear spin waves give $v_y = 0$.

9.3 Simulation model

The simulations run were similar to those in the previous chapter. The size of the sample and the cells were equal, and the initialisation of the AFM skyrmion occured in the same manner. The only difference in material properties was the damping constant, having been lowered to $\alpha = 0.001$ after a difficulty in obtaining stable magnons was observed in simulations done with $\alpha = 0.1$.

A single harmonic sinusoidal field was applied to the left-most 20 nm of the sample. The form of the magnetic field applied was

$$\mathbf{H}_{SW} = \left[H_0^x \sin(\omega t), H_0^y \cos(\omega t + \phi), 0\right] \tag{9.7}$$

Different polarisations were acchieved by varying the amplitudes H_0^x and H_0^y, and the phase of the y component ϕ. Four polarisations were simulated, demonstrated in figure 9.1.

The step time was set to have a maximum value of 1×10^{-14} seconds, again using the Dormand-Prince method [29]. The temperature of the system was set to 0 K in the inital conditions. Detecting the location of the skyrmion was done as described in Appendix B.

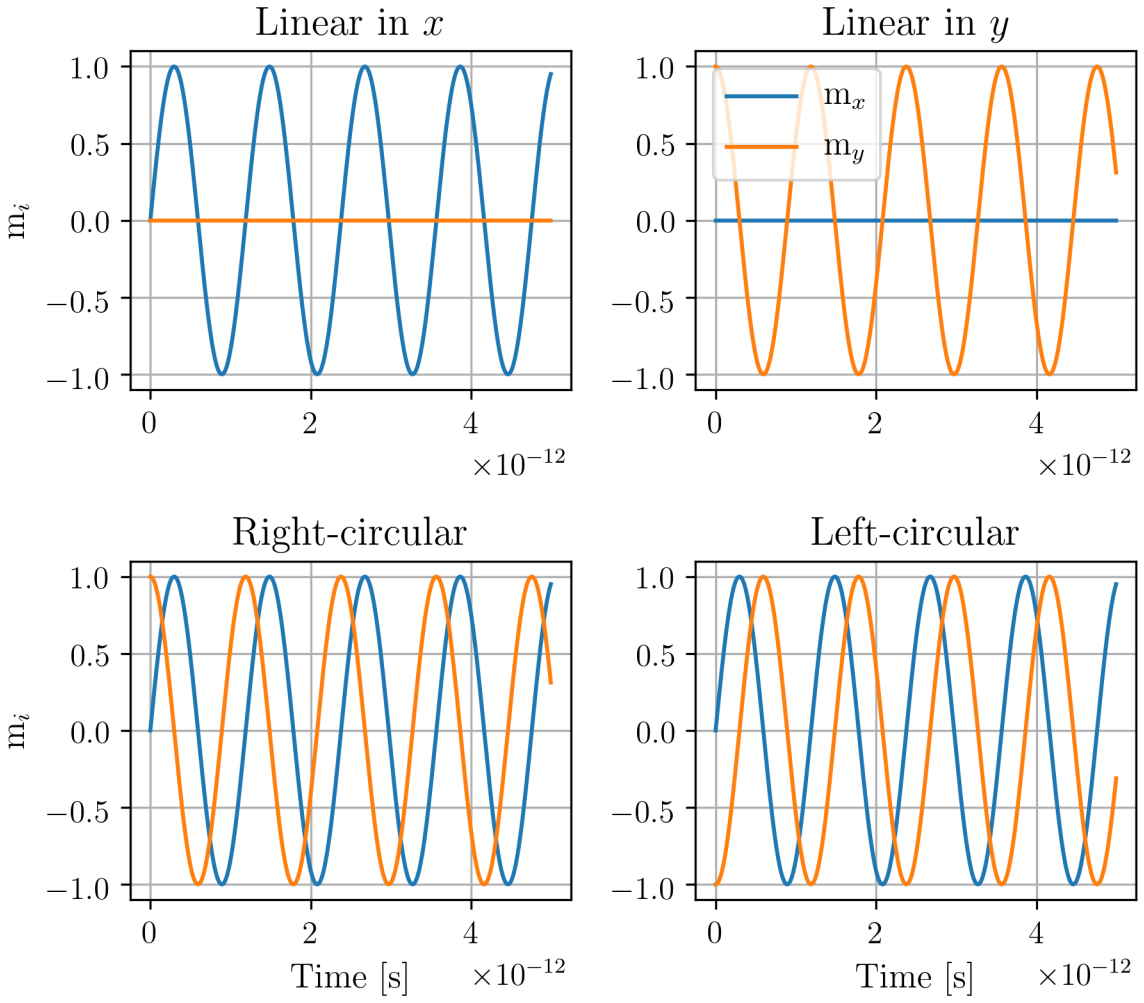

Figure 9.1: The shape of the magnetic fields which are applied to the antiferromagnetic material to induce spin waves. These shapes are multiplied with the amplitude H_0.

9.4 Verifying the spin waves

Before looking at the motion of the antiferromagnetic skyrmion, equivalent but uniform systems were investigated.

In an attempt to see the polarisation of the magnons, the magnetic moment of one spin was followed throughout the simulation. This was done for spins centered in y, and at five evenly spread out positions in x. The results during the first 5×10^{-12} seconds of motion at a spin location $x = 100$ nm are given in figure 9.2. It can be seen that both of the circular polarisation are transferred successfully from the applied magnetic field to the spin wave. With the applied linear fields, the induced spin waves appear linearly polarised in the opposite direction. With an oscillating magnetic field in the x direction applied, a spin wave polarised in the y-direction is obtained. The frequencies in figure 9.2 appear similar to the 5.288 THz which is applied.

The same simulation was also run for 5×10^{-11} seconds, as is presented in figure 9.3. While the phase differences between the x- and y-components maintain as they did in figure 9.2, the magnitude of the oscillations do not. For the applied magnetic fields which are circular and the x-linear one, the oscillations in y far exceed the oscillations in x, giving the spin waves a very long, elliptical polarisation. The spin wave induced by the magnetic field linear in y is the only one which significantly differs from the other three, maintaining a linear polarisation in x throughout the 5×10^{-11} seconds.

The y-component of the magnetisation for the circular fields, and at several positions along x, are shown in figure 9.4. It can in the figures be seen that the same frequency and phase appears to be kept at positions x $= 100 - 400$ nm. It appears that the sinusoidal shape is unstable at very low amplitudes, as it can be observed at all positions. The shape of the wave at x $= 500$ nm thus might be due to its weak strength.

A further observation from figure 9.4 is that the first peak in the right-circular spin wave appears to reach $x = 100$ nm after 2.887×10^{-11} seconds, and $x = 200$ nm after 4.311×10^{-11} seconds, when looking at the first sign of oscillation in the y-direction. This gives the velocity of the spin wave to be 7022 m/s. The equivalent value for the left-circular wave is found to be 7002 m/s.

The amplitude of the peak decreases as it moves from x $= 100$ nm to x $= 200$ nm, indicating the presence of damping, as expected. Considering the amplitude of the peaks, the decrease in those 100 nm is of 58% and 62% for the right-circular and left-circular waves respectively.

9.5 Results

Now having an antiferromagnetic skyrmion located in the centre of the sample as the initial spin configuration, the skyrmion position when exposed to spin waves is shown in figures 9.5, 9.7, 9.8 and 9.6.

In applying different amplitudes of the magnetic fields, it is seen that a stronger magnetic field induces faster motion. It appears that a maximum velocity is approached with $H_0 = 0.8$ T for the circular magnetic fields and the field linear in x, as the increase in velocity from $H_0 = 0.6$ T is small. The graphs also show that the velocity of the skyrmion decreases as it moves away from the region in which the spin waves are generated. Knowing from the previous section that the amplitude of the spin waves decays as they travel in space, this is as expected.

The resonance frequency $\omega_r = 5.288$ THz was found theoretically, and has been used throughout most of the simulations. A test was done with slightly varying input frequencies, as shown in figure 9.7. This confirmes that the maximum velocity of the skyrmions is closer to 5.288 THz than the other frequencies tested. A further factor which has

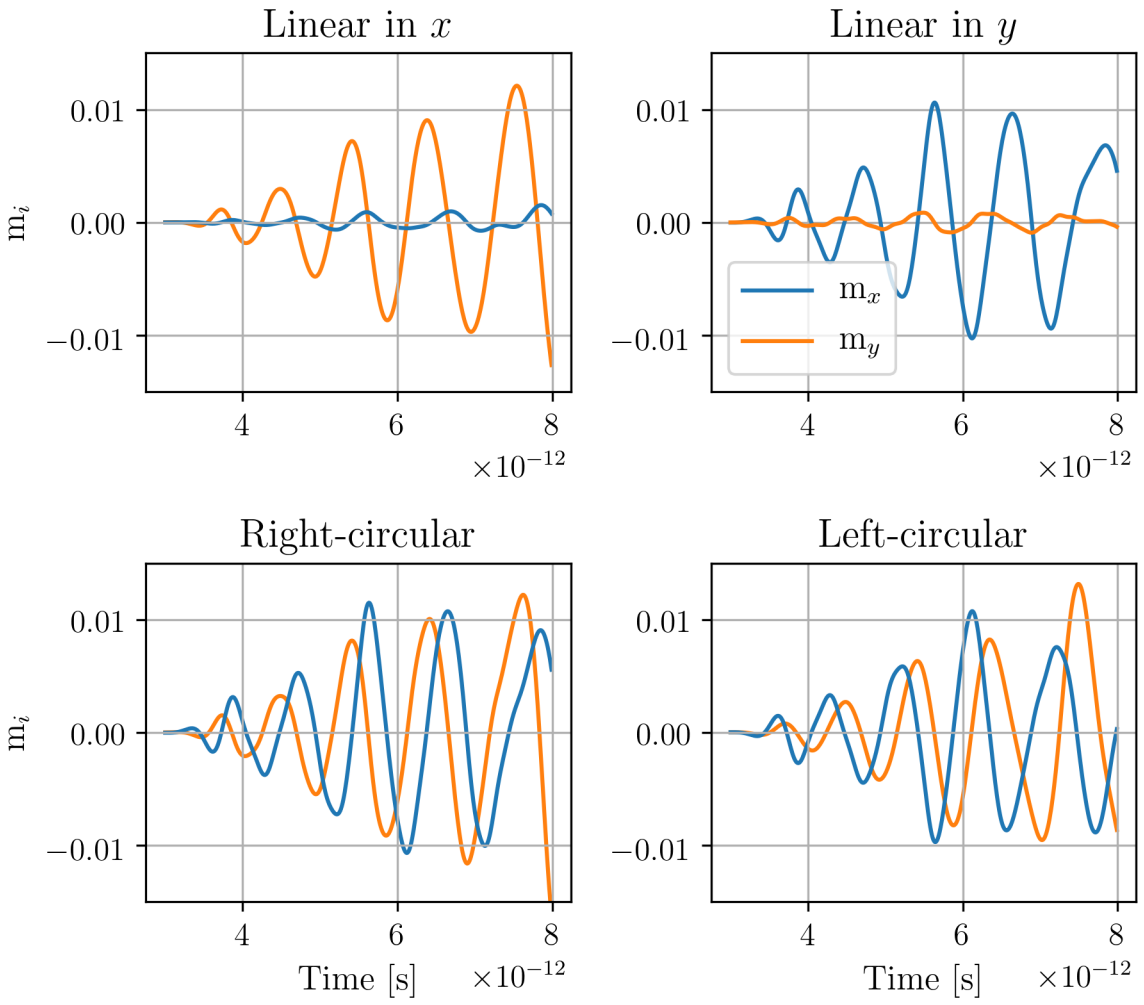

Figure 9.2: The x- and y-components of a magnetic moment located at $x = 100$ nm through 5×10^{-12} seconds. Different sinusoidal magnetic fields, both linear and circular, are applied between $x = 0$ and $x = 20$ nm, as is given in figure 9.1. The amplitude of all fields applied was 0.60 T, and the frequency was $\omega = 5.288$ THz.

tested was the width of the region generating the spin waves. The resulting motion of the skyrmions is shown in figure 9.8.

Of the four polarisations applied, the only one showing a significanty different behaviour than the others is the field linear in the y-direction. The skyrmion motion is for that field much slower than for the others. The average velocities of the skyrmions are given in table 9.1. For the simulations in which the skyrmions reached the end of the sample, and subsequently stayed in that position, the velocity is found as the average during the time in which the skyrmion was in motion. The movement in the y-direction was also measured in all simulations run. The most movement seen was ± 1 nm in the simulations with $H_0 = 0.8$ T, and for all simulations with lower field amplitudes applied there was zero movement in the y-direction.

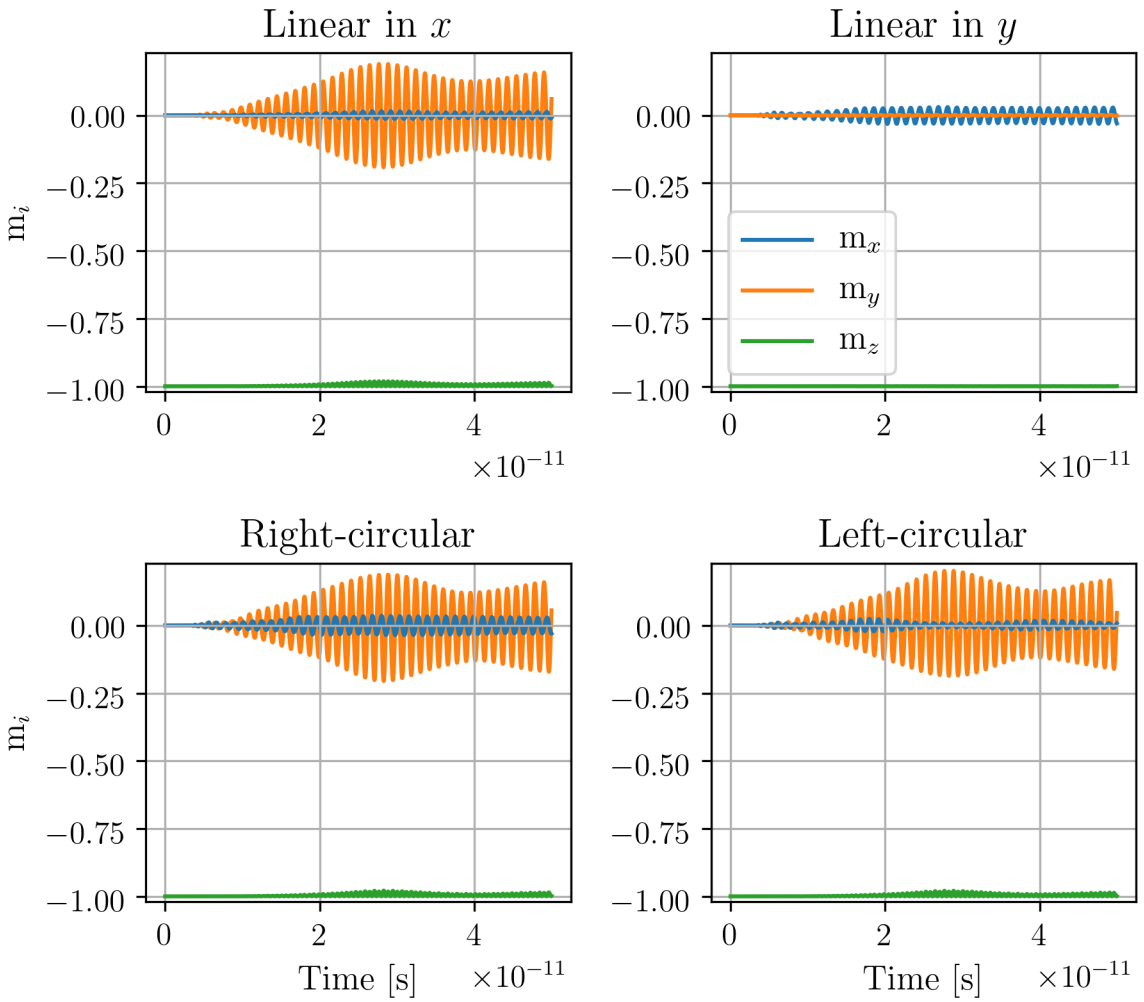

Figure 9.3: The x- and y-components of a magnetic moment located at $x = 100$ nm through 5×10^{-11} seconds. Different sinusoidal magnetic fields, both linear and circular, are applied between $x = 0$ and $x = 20$ nm, as is given in figure 9.1. The amplitude of all fields applied was 0.60 T, and the frequency was $\omega = 5.288$ THz.

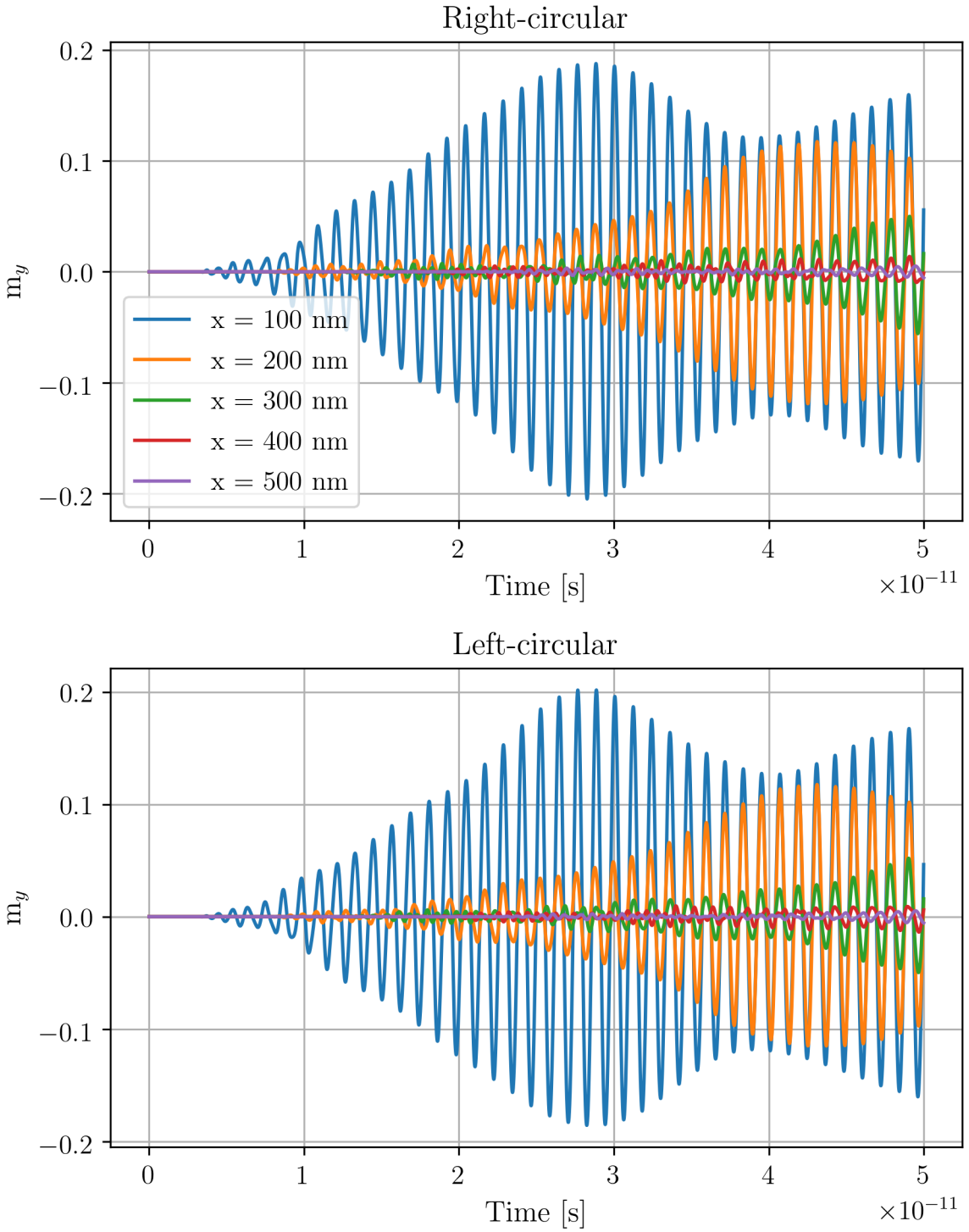

Figure 9.4: The y-component of magnetic moments positioned along the length of the sample, followed through 5×10^{-11} seconds. Circular sinusoidal magnetic fields are applied between $x = 0$ and $x = 20$ nm. The simulation is done with $H_0 = 0.6$ T and $\omega = 5.288$ THz.

		Polarisation			
		x-linear	y-linear	Right-circular	Left-circular
$\mathbf{H_0}$	0.2 T	25.45	0.69	25.75	25.75
	0.4 T	57.45	2.40	58.33	58.33
	0.6 T	103.23	4.41	89.30	89.30
	0.8 T	88.48	5.61	101.32	101.32

Table 9.1: The average velocities of skyrmions in the x-direction, induced by a localised magnetic field with polarisation as specified in the table. The unit of the velocities is m/s. The width of the region generating spin waves was 20 nm, and the frequency of the fields applied was $\omega = 5.288$ THz.

9.6 Discussion

The lack of movement by the skyrmions in the y-direction show that the spin waves, as seen from the discussion in section 9.4, were not circularly polarised. Based on the elliptical shape of the spin waves seen, some movement was expected. A possible explanation to the complete lack of such movement can be that the spin waves were only observed during the first 5×10^{-11} seconds, while the skyrmion motion was measured over 5×10^{-9} seconds. The relative size of the oscillations in the x- and y-components can have continued to change. Alternatively, the elliptical polarisation may have been similar enough in shape to a linear polarisation for the amount of transferred spin angular momentum to be zero.

A much further discussion of the effect of spin waves on antiferromagnetic skyrmion is difficult due to the nature of the spin waves. In comparing the motion caused by the y-circular field to the others, it is clear that the magnitude of the wave is the most significant factor for the velocity of the skyrmion, and that linear spin wave cause the skyrmion to move away from the spin wave source.

One suggested reason for the elliptical shape of the spin waves is the effect of the interfacial DMI present in the system. The interfacial DMI tilts the spins near boundaries in a direction perpendicular to the boundary, and thus prevent spin motion in that perpendicular direction. In the simulation, the magnetic field is applied to a region with dimensions $20 \times 128 \times 0.4$ nm. These dimensions make movement in the y-direction require less force, and therefore create spin waves with a larger oscillation in the y-direction.

Possible solutions for creating circular spin waves are to apply the magnetic field to a material without DMI. However, the interaction is neccesary for the stabilisation of the skyrmion, meaning that the spin waves would have to cross some boundary of material properties successfully. A more simple solution is to apply the magnetic field to a quadratic region, in which oscillations in both directions would be created with equal strength.

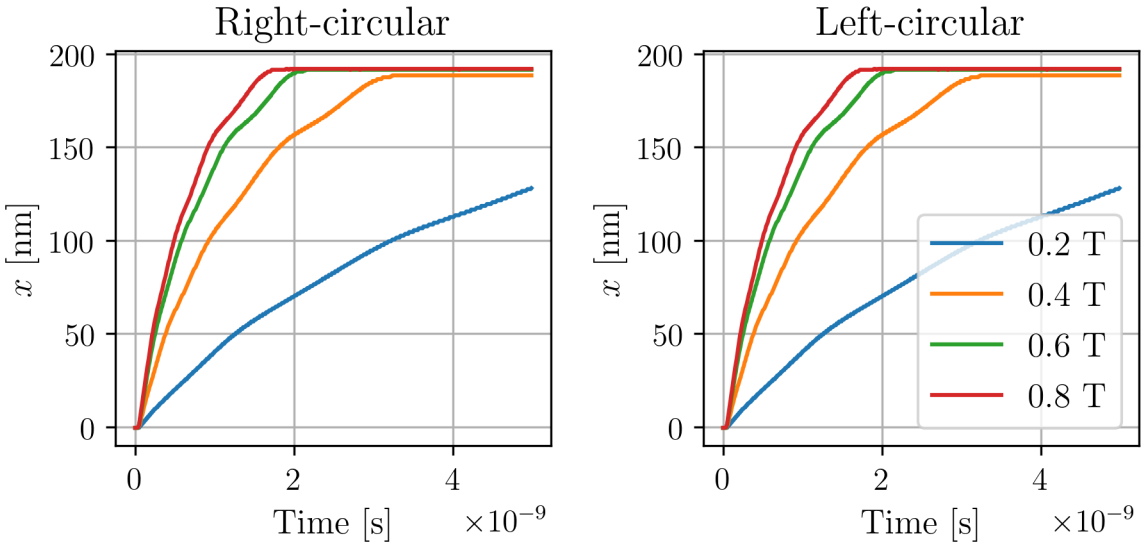

Figure 9.5: The position of AFM skyrmions exposed to spin waves induced by circularly polarised magnetic fields. The width of the region generating spin waves was 20 nm, and the frequency of the fields applied was $\omega = 5.288$ THz. The amplitude of the field was varied, and is given in the legend, which applies for both plots.

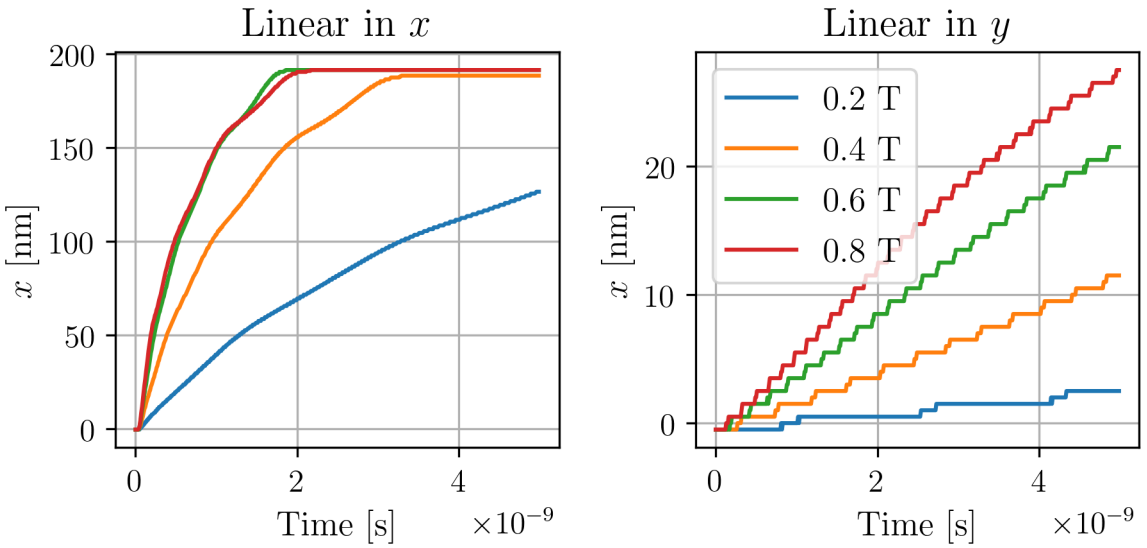

Figure 9.6: The position of AFM skyrmions exposed to spin waves induced by linearly polarised magnetic fields. The width of the region generating spin waves was 20 nm, and the frequency of the fields applied was $\omega = 5.288$ THz. The amplitude of the field was varied, and is given in the legend, which applies for both plots.

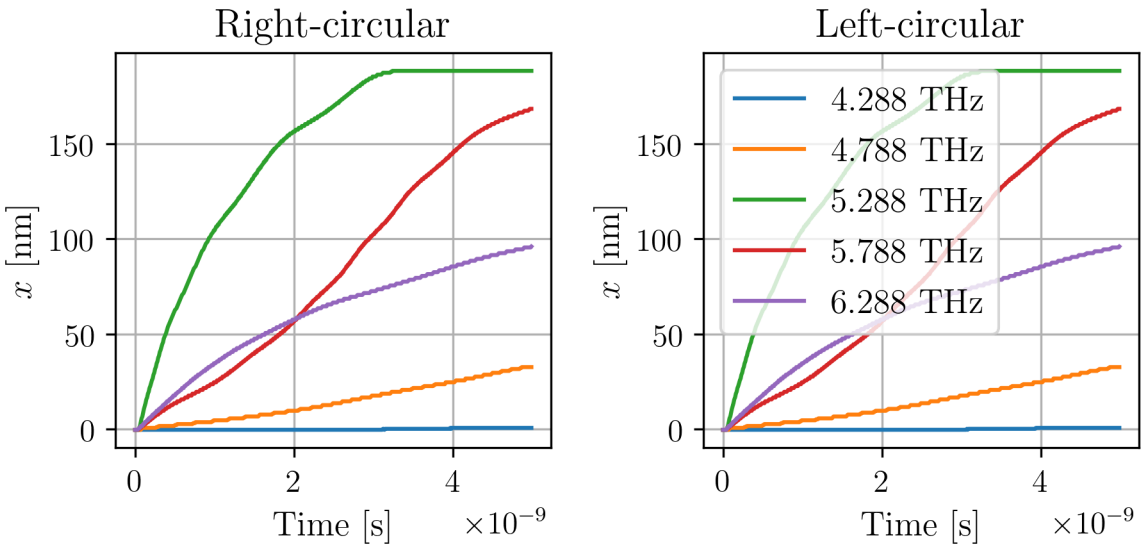

Figure 9.7: The position of AFM skyrmions exposed to spin waves induced by circularly polarised magnetic fields. The width of the region generating spin waves was 20 nm, and the amplitude of the fields applied was 0.4 T. The frequency of the fields was varied, and is given in the legend, which applies for both plots.

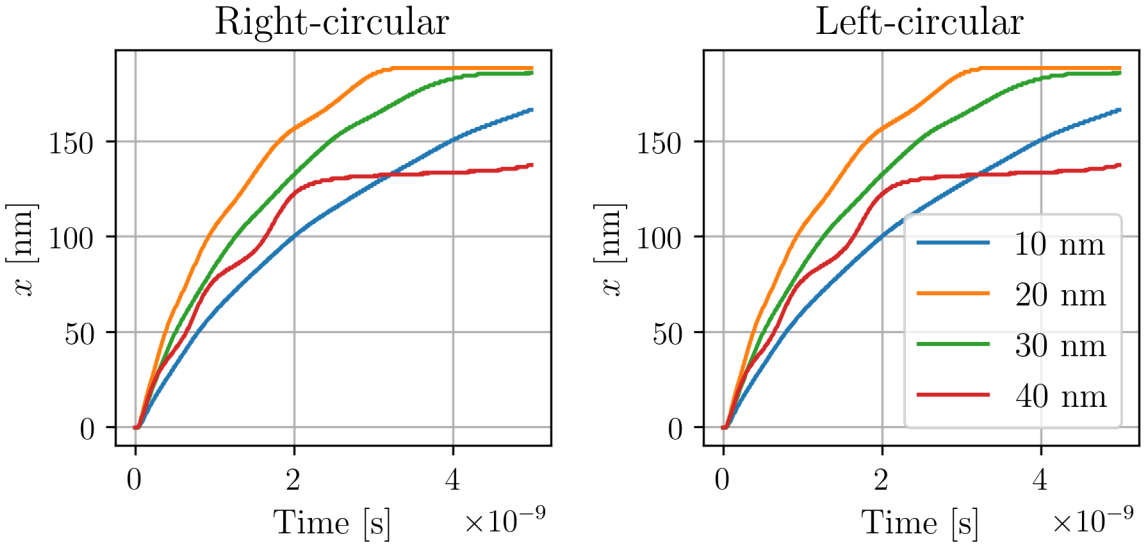

Figure 9.8: The position of AFM skyrmions exposed to spin waves induced by circularly polarised magnetic fields. The amplitude of the fields applied was 0.4 T, and the frequency was $\omega = 5.288$ THz. The width of the region renerating the spin waves was varied, and is given in the legend, which applies for both plots.

Chapter 10

Conclusions and further work

Throughout the work for this thesis, the motion of antiferromagnetic skyrmions exposed to spin waves has been studied. The motion has been found to be faster with spin waves induced by a local magnetic field than with spin waves induced by a thermal gradient, with maximum observed velocities of 103.2 m/s and 8.9 m/s, respectively. The former is also a deterministic process, and thus more reliable than the thermal fluctuations involved in the latter. Both processes induce significant motion only along the x-direction. Circularly polarised spin waves have been predicted to induce motion also in the y-direction, but this was not successfully achieved in simulations

Different damping constants are used in the two simulations. The temperature gradient simulations have $\alpha = 0.1$, while the magnetic field simulations have $\alpha = 0.001$. Increasing the damping constant in the latter is expected to increase the rate of decay of the spin waves, which in turn should decrease the velocity of the skyrmion.

In considering further work, the generation of spin waves with a localised magnetic field in general requires further studies. The two solutions suggested in 9.5 to obtaining circularly polarised spin have not been tested numerically due to lack of time, but should be simple to do in mumax3.

The processes involving magnetically induced spin waves are all done at zero temperature. In the temperature gradient simulations, the lower temperature in the sample is also zero kelvin. An important step towards using antiferromagnetic skyrmions in practical spintronics applications will be to develop the theory for higher temperatures.

Future work should also consider canted antiferromagnetic systems. In this thesis, all models of antiferromagnets have assumed an antiparallel spin configuration as the ground state. The Dzyaloshinskii-Moriya interaction will however not only cause the stabilisation of the skyrmion, but will be relevant in all considerations of the material.

Appendices

Appendix A

Initialising AFM skyrmions in mumax3

While ferromagnetic skyrmions can be initialised with a mumax3 function, a antiferromagnetic one must be created. This can be done by setting the initial magnetisation in each cell of the sample. The following function was used

```
for i:=0; i<Nx; i++{

  for j:=0; j<Ny; j++{

    r:=(exp(sqrt((i-Nx/2+0.5)*(i-Nx/2+0.5)+...
        ...(j-Ny/2+0.5)*(j-Ny/2+0.5))/9.6)-1)/(exp(30/9.6)-1);

        phi:=atan2((j-Ny/2+0.5),(i-Nx/2+0.5));

        mzansatz := (1-r*r)/(1+r*r);
        mxansatz := 2*r/(1+r*r)*cos(phi);
        myansatz := 2*r/(1+r*r)*sin(phi);

        if mod(i+j,2) == 0{
          m.setCell(i,j,0,vector(mxansatz,myansatz,mzansatz))
        } else {
          m.setCell(i,j,0,vector(-mxansatz,-myansatz,-mzansatz))
        }
  }
}
```

where Nx and Ny are the number of cells in the x and y directions. The magnetisation of a simulation can also be set by the .ovf-files produced by previous simulations. The resulting configuration from the above function is given in A.1, being a relaxed skyrmion. The size will is set by the material parameters otherwise defined in the input file, and will

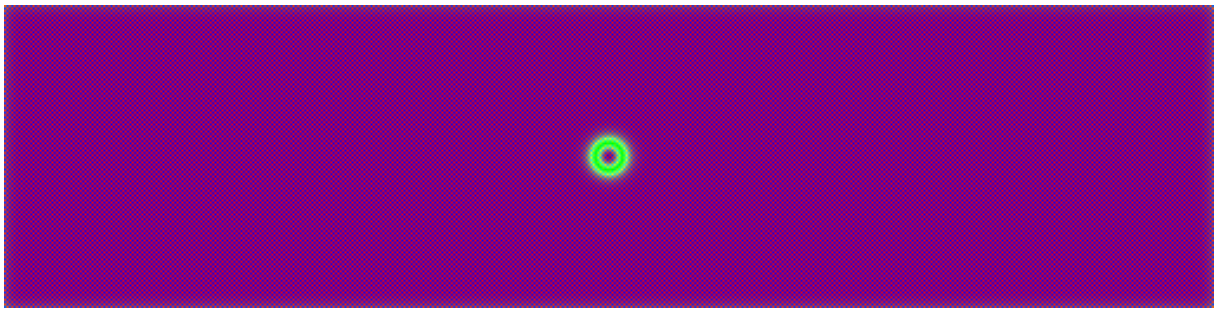

Figure A.1: An initialised AFM skyrmion in mumax3, here showed through its z component. The purple is really alternating red and blue cells, representing ± 1. Green represents the z component being 0.

thus generally not be equal to that in the figure.

Appendix B

Determining AFM skyrmion position in mumax3

For ferromagnetic systems, mumax3 offers a built-in function for finding the position of skyrmions. However, as mumax3 is not created with antiferromagnets in mind, no equivalent function for AFMs is available. The follow method was thus used, based on finding the approximate position of the skyrmion domain wall while assuming the skyrmion keeps a circular shape.

1. Define the spin values by which the skyrmion domain wall will be defined. As the samples looked have had uniform material defined by $m_z = \pm 1$, spin values $-0.1 < m_z < 0.1$ have been used.

2. Also define a region in which to look for the skyrmion. This is done to avoid detecting the walls of the sample, which due to DMI will have spins withing the abovecreated limits. The region is defined through a number l, where the region searched will then be the previous position of the skyrmion $\pm l$ in both x and y.

3. Loop through each cell in the file. If the cell is within the region as defined in point 2, consider its spin value. Save the minimum and maximum positions in which the spin value is within the domain wall.

4. The skyrmion should now be located with its center in the midpositions between the minimas and maximas found.

Bibliography

[1] Bernard Marr. *How Much Data Do We Create Every Day? The Mind-Blowing Stats Everyone Should Read*. https://www.forbes.com/sites/bernardmarr/2018/05/21/how-much-data-do-we-create-every-day-the-mind-blowing-stats-everyone-should-read/. Accessed on 2019-05-20. May 2019.

[2] Radoslav Danilak. *Why Energy Is A Big And Rapidly Growing Problem For Data Centers*. https://www.forbes.com/sites/forbestechcouncil/2017/12/15/why-energy-is-a-big-and-rapidly-growing-problem-for-data-centers/. Accessed on 2019-06-10. Dec. 2017.

[3] Steinar Brandslet. *Norsk gjennombrudd i spinnstrøm-teknologien kan gi oss datamaskiner som knapt bruker strøm*. https://www.tu.no/artikler/forskning-norsk-gjennombrudd-i-spinnstrom-teknologien-kan-gi-oss-datamaskiner-som-knapt-bruker-strom/445959. Sept. 2018.

[4] Editorial. "Skyrmion makeover". In: *Nature* 465 (2010). DOI: 10.1038/465846a.

[5] J. P. Liu, Z Zhang, and G. Zhao. *Skyrmions. Topological Structures, Properties, and Applications*. CRC Press, 2017.

[6] S. S. P. Parkin, M. Hayashi, and L. Thormas. "Magnetic Domain-Wall Racetrack Memory". In: *Science* 320.5873 (Apr. 2008). DOI: 10.1126/science.1145799.

[7] G. E. Uhlenbeck and S. Goudsmit. "Ersetzung der Hypothese vom unmechanischen Zwang durch eine Forderung bezüglich des inneren Verhaltens jedes einzelnen Elektrons". In: *Die Naturwissenschaften* 13.47 (Nov. 1925). DOI: 10.1007/BF01558878.

[8] S. Goudsmit. *The discovery of the electron spin*. https://www.lorentz.leidenuniv.nl/history/spin/goudsmit.html. Apr. 1971.

[9] D. J. Griffiths. *Introduction to Quantum Mechanics. Second Edition*. Pearson Education, Inc., 2005.

[10] Lars André Kristiansen. "Spin-orbit-induced dynamics of magnetic textures". MA thesis. Norwegian University of Science and Technology, 2017.

[11] Charles Kittel. *Introduction to Solid State Physics. Eight Edition*. John Wiley & Sons, Inc., 2005.

[12] Xingxing Li and Jinlong Yang. "First-principles design of spintronics materials". In: *National Science Review* 3.1 (Apr. 2016), pp. 365–381. DOI: 10.1093/nsr/nww026.

[13] H. Y. Yuan et al. "Classification of magnetic forces acting on an antiferromagnetic domain wall". In: *Physical Review B* 97.214434 (2018). DOI: 10.1103/PhysRevB.97.214434.

[14] Olle Eriksson et al. *Atomistic Spin Dynamics: Foundations and Applications*. Oxford University Press, 2017.

[15] Bangalore Indian Institute of Science. *Heisenberg and Ferromagnetism*. https://www.ias.ac.in/article/fulltext/reso/009/08/0057-0066. Accessed on 2019-05-09. Aug. 2004.

[16] Bram van Dijk. "Skyrmions and the Dzyaloshinskii-Moriya Interaction". MA thesis. Utrecht University, 2014.

[17] Alex Hubert and Rudolf Schäfer. *Magnetic Domains. The analysis of Magnetic Microstructures*. Springer Verlag, 2009.

[18] Alexander Makarov. "Modeling of Emerging Resistive Switching Based Memory Cells". PhD thesis. Technische Universität Wien, 2014.

[19] Arne Brataas, Andrew D. Kent, and Hideo Ohno. "Current-induced torques in magnetic materials". In: *Nature Materials* 11.5 (Apr. 2012), pp. 372–381. DOI: 10.1038/nmat3311.

[20] Helmut Fõll. *4.3.4 Domain Movement in External Fields*. https://www.tf.uni-kiel.de/matwis/amat/elmat_en/kap_4/backbone/r4_3_4.html. Accessed on 2018-11-26.

[21] S. S. P. Parkin, M. Hayashi, and L. Thomas. "Magnetic Domain-Wall Racetrack Memory". In: *Science* 320.190 (2008). DOI: 10.1126/science.1145799.

[22] X. S. Wang, H. Y. Yuan, and Y. R. Wang. "A theory on skyrmion size". In: *Communications Physics* 1 (July 2018). DOI: 10.1038/s42005-018-0029-0.

[23] Gong Chen. "Skyrmion Hall effect". In: *Nature Physics* 13 (Jan. 2017).

[24] M. B. A. Jalilab et al. *Stability of topological charge of magnetic skyrmion configurations*. May 2016. DOI: https://doi.org/10.1016/j.jmmm.2015.09.064.

[25] E. G. Tveten, A. Qaiumzadeh, and A. Brataas. "Antiferromagnetic Domain Wall Motion Induced by Spin Waves". In: *Physical Review Letters* 112 (2014). DOI: 10.1103/PhysRevLett.112.147204.

[26] University of Groningen. *Magnon Spintronics*. https://www.rug.nl/research/zernike/physics-of-nanodevices/research/magnonspintronics. Accessed on 2019-05-09. Aug. 2016.

[27] Pablo Nieves. *Micromagnetic models for high-temperature magnetization dynamics*. May 2015. DOI: 10.13140/RG.2.1.4349.1682.

[28] R. F. L. Evans1 et al. "Atomistic spin model simulations of magnetic nanomaterials". In: *Journal of Physics: Condensed Matter* 26.10 (Feb. 2014). DOI: 10.1088/0953-8984/26/10/103202.

[29] Arne Vansteenkiste et al. "The design and verification of mumax3". In: *AIP Advances* 4.10 (June 2014). DOI: 10.1063/1.4899186.

[30] Henrik Enoksen. "Quantum Transport in Hybrid Structures". PhD thesis. Norwegian University of Science and Technology, 2013.

[31] J. Sampaio et al. "Nucleation, stability and current-induced motion of isolated magnetic skyrmions in nanostructures". In: *Nature Nanotechnology* 8.11 (Oct. 2013). DOI: 10.1038/nnano.2013.210.

[32] O. Gomonay et al. "Antiferromagnetic spin textures and dynamics". In: *Nature Physics* 14 (2018). DOI: 10.1038/s41567-018-0049-4.

[33] Rohollah Koshlahni et al. "Ultrafast generation and dynamics of isolated skyrmions in antiferromagnetic insulators". In: *Physical Review B* (Feb. 2019). DOI: 10.1103/PhysRevB.99.054423.

[34] Ken A. Dill and Sarina Bromberg. *Molecular Driving Forces. Statistical Thermodynamics in Biology, Chemistry, Physics, and Nanosciencee. Second Edition.* Garland Science, 2011.

[35] A. A. Thiele. "Steady-State Motion of Magnetic Domains". In: *Physical Review Letters* 30.6 (1973). DOI: 10.1103/PhysRevLett.30.230.

[36] S.-Z. Lin. "Dynamics and inertia of a skyrmion in chiral magnets and interfaces: A linear response approach based on magnon excitations". In: *Phys. Rev. B* 96.014407 (2017).

[37] J Ding, X. Yang, and T. Zhu. "The Motion of Magnetic Skyrmions Driven by Propagating Spin Waves". In: *IEEE Transactions on Magnetics* 51.11 (2015).

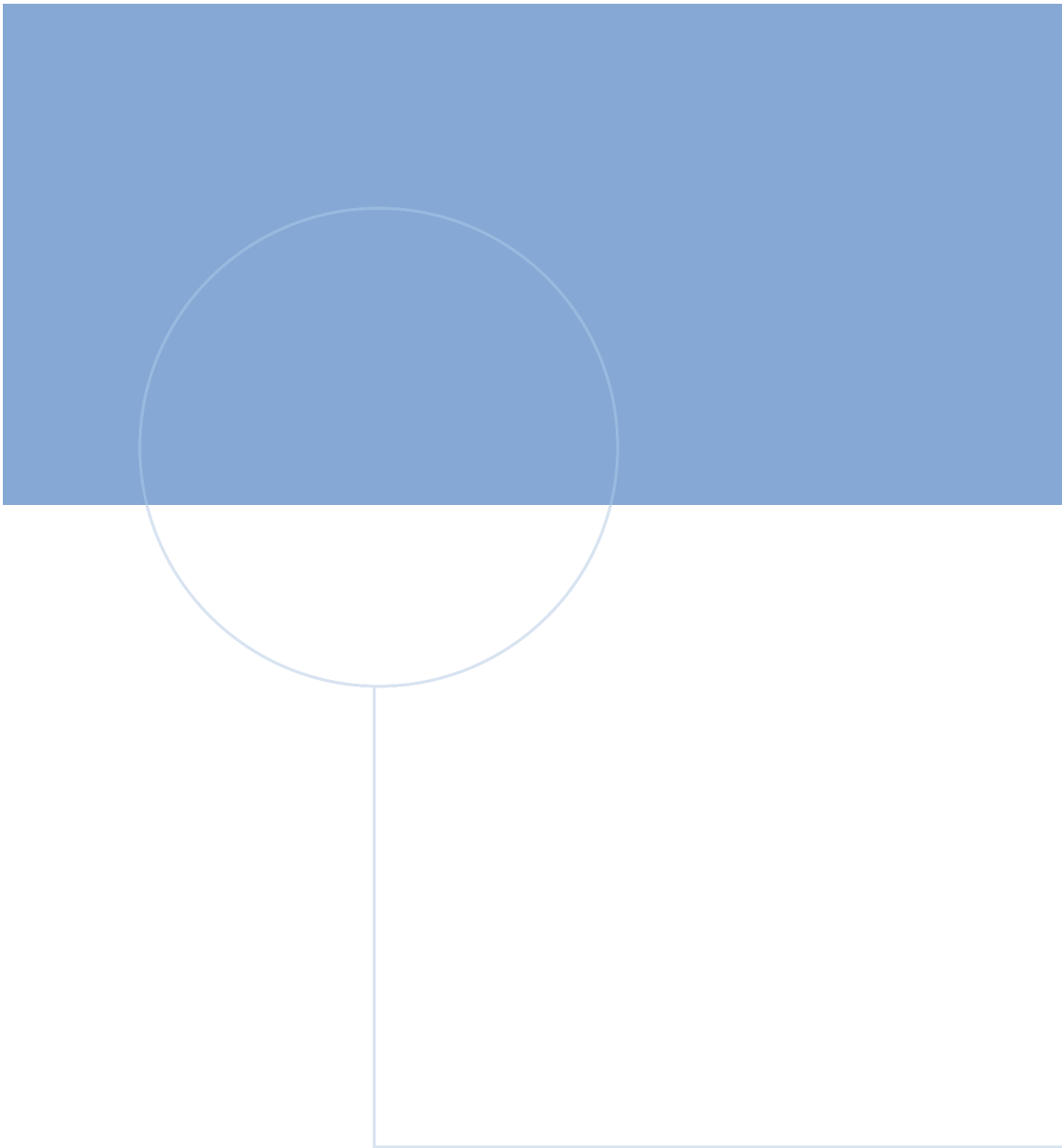

NTNU
Norwegian University of
Science and Technology